



1 **Differences in aerosol and cloud properties along the central**
2 **California coast when winds change from northerly to southerly**

3

4 Kira Zeider¹, Grace Betito², Anthony Bucholtz³, Peng Xian⁴, Annette Walker⁴, Armin
5 Sorooshian^{1,2*}

6

7 ¹Department of Chemical and Environmental Engineering, University of Arizona, Tucson, Arizona, 85721, USA

8 ²Department of Hydrology and Atmospheric Sciences, University of Arizona, Tucson, Arizona, 85721, USA

9 ³Department of Meteorology, Naval Postgraduate School, Monterey, California, 93943, USA

10 ⁴Marine Meteorology Division, Naval Research Laboratory, Monterey, California, 93943, USA

11

12

13 **Correspondence to:* Armin Sorooshian (armin@arizona.edu)

14

15



16 **Abstract.** Wind reversals resulting in southerly flow along the California coast are not well understood in terms of
17 how aerosol and cloud characteristics change. This gap is addressed using airborne field measurements enhanced with
18 data from space-borne remote sensing (Moderate Resolution Imaging Spectroradiometer), surface stations
19 (Interagency Monitoring of Protected Visual Environments), and models (Navy Aerosol Analysis and Prediction
20 System and Coupled Ocean/Atmosphere Mesoscale Prediction System), with a focus on sub- and supermicron aerosol,
21 and cloud microphysical variables: cloud droplet number concentration (N_d), cloud optical thickness (COT), and cloud
22 droplet effective radius (r_e). Southerly flow coincided with higher values of submicron aerosol concentration (N_a) and
23 mass concentrations of species representative of fine aerosol pollution (NO_3^- and nss-SO_4^{2-}) and shipping/continental
24 emissions (V, oxalate, NH_4^+ , Ni, OC, and EC). Supermicron N_a did not change, however, heightened levels of acidic
25 species in southerly flow coincided with reduced $\text{Cl}^-:\text{Na}^+$ suggestive of Cl depletion in salt particles. Clouds responded
26 correspondingly in southerly flow, with more acidic cloud water, higher levels of similar species as in the aerosol
27 phase (e.g., NO_3^- , nss-SO_4^{2-} , NH_4^+ , V), along with elevated values of N_d and COT and reduced r_e during campaigns
28 with similar cloud liquid water paths. Case study flights help to visualize offshore pollution gradients and highlight
29 the sensitivity of the results to the presence of widespread smoke coverage including how associated plumes have
30 enhanced supermicron N_a . These results have implications for aerosol-cloud interactions during wind reversals, and
31 have relevance for weather, public welfare, and aviation.



32 1 Introduction

33 The northeastern Pacific Ocean is one of the most heavily studied regions as it relates to aerosol-cloud
34 interactions due to the persistent and spatially broad stratocumulus cloud deck that is influenced by a variety of
35 emissions sources, notably shipping (Wood, 2012; Russell et al., 2013). One aspect of that region that warrants more
36 attention is the predominant direction of lower tropospheric winds, as recent work has suggested that it can have
37 significant implications for aerosol and cloud properties (Juliano et al., 2019a; 2019b). The wind direction along the
38 North American west coast is influenced by its topography, namely the coastal mountains (e.g., National Research
39 Council, 1992), and during the California (CA) warm season (April through September), it is primarily from the north
40 along the coast. An important weather phenomenon during that season is the infrequent and short-lived (from one to
41 several days) transition from northerly to southerly flow near the coast up to 100 km offshore (e.g., Nuss et al., 2000).
42 Particularly, the northerly winds weaken (e.g., Winant et al., 1987; Melton et al., 2009) and eventually reverse. Along
43 with a decrease in temperature and increases in pressure and cloud fraction (e.g., increases in low clouds and fog),
44 there is also a change in overall wind speed: most northerlies (~75%) have a wind speed component less than 5 m s^{-1}
45 (Bond et al., 1996), whereas southerly “surges” are characterized by sudden increases in wind speed to 15 m s^{-1} or
46 greater (Mass and Albright, 1987). This is not a phenomenon that is unique to the U.S.; a handful of studies have noted
47 these events along the coasts of South America (e.g., Garreaud et al., 2002; Garreaud and Rutllant, 2003), southern
48 Africa (e.g., Reason and Jury, 1990), and even Australia (e.g., Holland and Leslie, 1986; Reason et al., 1999; Reid
49 and Leslie, 1999).

50 These wind reversals – referred to as either coastally trapped disturbances (CTDs), coastally trapped wind
51 reversals (CTWRs), stratus surges, or southerly surges, to name a few – have been studied since the 1970s (Gill, 1977;
52 Dorman, 1985). There have been a fair number of publications discussing the dynamics and forcing mechanisms for
53 such events (thoroughly reviewed by Nuss et al., 2000) primarily using data from buoys, radars, and research aircraft.
54 Buoy (e.g., Bond et al., 1996) and satellite studies (e.g., Parish, 2000; Rahn and Parish, 2010) mainly discussed the
55 topics related to mesoscale structure, while the research aircraft studies (e.g., Ralph et al., 1998; Rahn and Parish,
56 2007) have attempted to document physical characteristics of the wind reversal. For example, Rahn and Parish (2007)
57 used sawtooth maneuvers to depict the vertical structure of the 22-25 June 2006 reversal through examining surface
58 pressure, temperature, wind direction, wind speed, along-shore wind, and cross-shore wind. Additionally, there have
59 been multiple studies attempting to model these wind reversals (e.g., Rogerson and Samelson, 1995; Guan et al., 1998;
60 Skamarock et al., 1999; Mass and Steenburgh, 2000; Thompson et al., 2005) to better understand their initiation,
61 propagation, and cessation. These studies found that CTDs are initiated by changes in synoptic-scale flow, particularly
62 offshore, and that the coastal mountains dampen the flow, deepen the marine layer, and propagate a mesoscale coastal
63 ridge of higher pressure northward that ultimately leads to the development of a coastally trapped southerly wind
64 component.

65 However, there have been limited attempts to look into aerosol and cloud characteristics during a southerly
66 surge (e.g., Juliano et al., 2019a; 2019b), and among them were studies that happened to encounter them by chance
67 without these surges having been the study’s focus (Crosbie et al., 2016; Dadashazar et al., 2020). Juliano et al. (2019a)
68 was, to our best knowledge, the first study to focus on CTD aerosol-cloud interactions using 23 cases identified
69 between 2004 and 2016 with buoy data and satellite imagery. They found notable differing characteristics between
70 non-CTD (northerly flow) and CTD (southerly flow) conditions, with higher cloud droplet number concentration (N_d)
71 and lower droplet effective radius (r_e) for CTD cases. Compared to non-CTD events, CTD events had r_e values that
72 were ~20-40% lower (i.e., differences often exceeding ~3 μm) and N_d values (~250 cm^{-3}) that were almost twice as
73 large in many areas. They attributed this to some combination of (i) mixing of sea salt particles into the boundary layer
74 due to an observed wind stress-sea surface temperature cycle; (ii) offshore flow transporting continental aerosol into
75 areas offshore of CA; and (iii) extended periods of time that southerly air spends in shipping lanes. Some continental
76 sources they noted include agricultural emissions from the CA Central Valley, biogenic emissions from various major
77 sources such as forests around Oregon and northern CA, smoke from biomass burning, and urban emissions from
78 major CA cities such as Los Angeles, San Jose, Sacramento, and San Francisco. These sources have been confirmed
79 in various studies conducted in coastal areas of central CA (Wang et al., 2014; Maudlin et al., 2015; Braun et al., 2017;
80 Dadashazar et al., 2019; Ma et al., 2019). A subsequent study (Juliano et al., 2019b) analyzed three CTD events using
81 satellite and aircraft observations, as well as numerical simulations. That study’s usage of aircraft data was limited to
82 cloud water composition, to support results from their previous study that non-CTD days were primarily influenced
83 by marine sources like sea salt, whereas CTD days exhibited more relative influence from continental and shipping



84 (i.e., higher SO_4^{2-} and NO_3^-) sources. Those studies noted that additional observations, specifically of an in situ nature,
85 were needed to confirm results that were mostly based on modeling and remote sensing.

86 The goal of this study is to contrast aerosol and cloud characteristics between southerly and northerly flow
87 regimes in the lower troposphere (below 3 km) offshore of central CA. Note that we do not focus here on
88 meteorological and large-scale features associated with wind reversals and do not classify events based on whether
89 they are CTDs but focus exclusively on boundary layer wind direction. As a way to address the shortage of in situ
90 observational data used for this research application, an important inventory of airborne data are leveraged that have
91 been collected over the last two decades (Sorooshian et al., 2018) that afford increased statistics of southerly flow
92 cases relative to Juliano et al. (2019b). Such cases are difficult to sample owing to their lower frequencies (Table 1)
93 compared to days with northerly flow and because aircraft flights do not occur each day, so some southerly cases are
94 missed during airborne campaigns. In total, 17 days of data exist from Naval Postgraduate School (NPS) Twin Otter
95 campaigns coinciding with southerly flow, with some days including multiple flights. One thing that has yet to happen
96 in past studies is to use in situ data to compare more than just cloud water composition but also relevant variables such
97 as aerosol number concentration (N_a) and N_d , which is crucial to intercompare with satellite data and put previous
98 speculations about aerosol and cloud responses to southerly flow on sturdier ground. As the aircraft data are still
99 limited, we complement the analysis with other datasets, including those from satellite remote sensors, models, and
100 surface stations.

101 The structure of this paper is as follows: Sect. 2 reports on methods used; Sect. 3 shows results beginning
102 with a discussion of how well a model can represent southerly winds, followed by assessing how well the datasets
103 show more fine pollution during southerly days and if clouds respond accordingly with the usual chain of events
104 associated with the Twomey effect (Twomey, 1974) whereby clouds have more but smaller drops at similar liquid
105 water path; and Sect. 4 provides conclusions. The results of this work have implications for numerous societal and
106 environmental factors sensitive to aerosol and cloud characteristics such as transportation (especially aviation),
107 agriculture, biogeochemical cycling of nutrients and contaminants, and coastal ecology (Dadashazar et al., 2020).

109 2 Methods

110 This study relies on the use of multiple datasets to examine how aerosol and cloud characteristics vary
111 between traditional northerly flow along the CA coastline as compared to less common southerly flow periods. This
112 study was initially inspired by airborne field measurements (Table 1) whereby on a few opportune flight days,
113 southerly flow was encountered off the CA coast. Because these events were rare in comparison to the majority of
114 flights with northerly flow (Southerly Winds % in Table 1), several campaigns worth of data are compiled to build
115 more statistics of southerly flow days. The airborne data used here are all from summer periods, which is when most
116 field studies have focused on this region to investigate aerosol-cloud interactions (e.g., Russell et al., 2013) allowing
117 for easier intercomparison for interested readers. We enhance statistics by also conducting complementary analyses
118 with data obtained from space-borne remote sensing, surface-based stations, and models. Below we first describe the
119 airborne datasets, followed by the wind classification method, and then descriptions of the models, surface data, and
120 satellite data.

122 2.1 Airborne Field Missions

123 This study utilizes data from six airborne missions based out of Marina, CA (Fig. 1) using the Naval
124 Postgraduate School (NPS) Twin Otter aircraft. The scientific target of these campaigns included a mix of aerosol-
125 cloud interactions, aerosol microphysical processes, and characterization of wildfire emissions: the Eastern Pacific
126 Emitted Aerosol Cloud Experiment (E-PEACE), the Nucleation in California Experiment (NiCE), the Biological and
127 Oceanic Atmospheric Study (BOAS), the Fog and Stratocumulus Evolution Experiment (FASE), the Marine Aerosol
128 Cloud And Wildfire Study (MACAWS), and the California Smoke Mission (CSM) (Table 1). Another Twin Otter
129 mission from 2019 (Monterey Aerosol Research Campaign - MONARC) is not included in this analysis due to the
130 lack of southerly flow days sampled during the campaign. The research flight (RF) paths for each campaign are shown
131 in Fig. 1. In some instances, multiple flights were conducted on a single day, either to capture time-sensitive
132 atmospheric features or to collect data beyond the endurance limit of the instrumented aircraft. For those days, RFs
133 are assigned the same number but are distinguished with endings 'A,' 'B,' and 'C,' for successive flights, respectively.
134 E-PEACE and NiCE had the most cases of southerly flow owing partly to those campaigns having had the most flights:
135 five out of 30 flights for E-PEACE; four out of 23 flights for NiCE. BOAS also had four flights with southerly flow



136 (out of 15 flights) but they were spread across two flights days as compared to E-PEACE and NiCE whose southerly
 137 flights were all on distinct days.

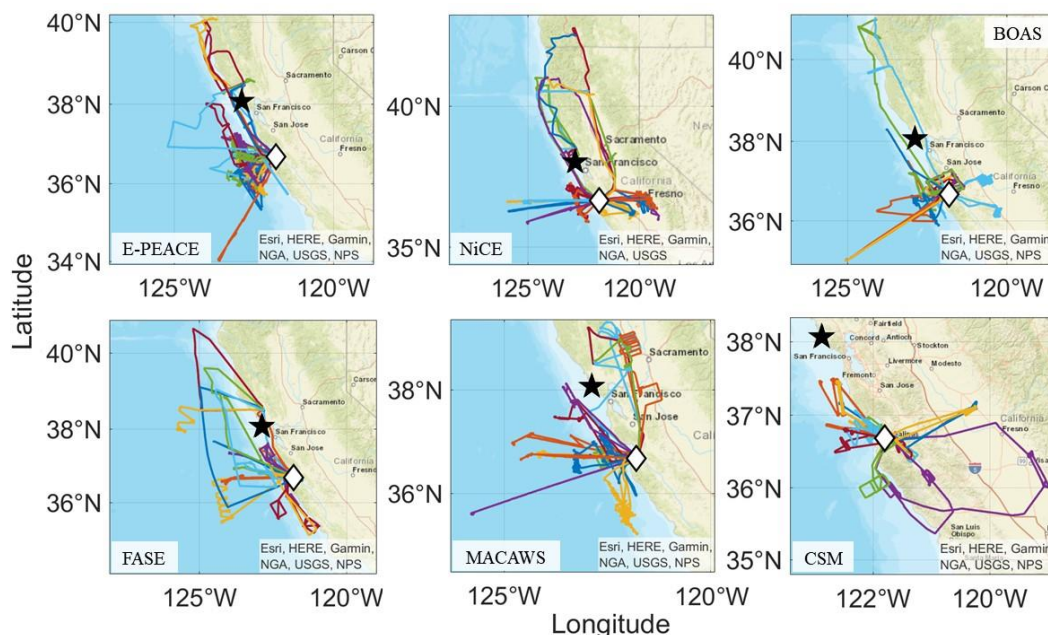
138 The Twin Otter flew at $\sim 55 \text{ m s}^{-1}$ and conducted measurements during level legs and sounding profiles, over
 139 both the land and the ocean, and within and above the boundary layer during flight periods ranging from one to five
 140 hours. Additional information regarding aircraft and flight characteristics, as well as the general flight strategy is
 141 summarized in Sorooshian et al. (2019). The general area of focus in this study was within the following range of
 142 coordinates, with many of the results specifically targeting just the ocean areas in this spatial domain: $35.31^\circ \text{ N} -$
 143 40.99° N , $125.93^\circ \text{ W} - 118.98^\circ \text{ W}$.

144

145 **Table 1: Summary of NPS Twin Otter campaigns used in this study, including dates, number of RFs per campaign, RFs**
 146 **that are categorized as having had southerly flow, and percentage of southerly days during the campaign period (including**
 147 **all days in those months and not just RF days). Days are categorized as having southerly flow based on the analysis in Sect.**
 148 **2.2.**

Campaign	Dates	Total RFs	RF # (Flight Date) with Southerly Winds	Southerly Winds % (# Southerly days / Total days in period)
E-PEACE	07/08 – 08/18/2011	30	RF11 (07/23), RF12 (07/24), RF14 (07/27), RF15 (07/28), RF16 (07/29)	12.90% (8/62)
NiCE	07/08 – 08/07/2013	23	RF7 (07/16), RF8 (07/17), RF9 (07/18), RF16 (07/29)	14.52% (9/62)
BOAS	07/02 – 07/24/2015	15	RF10A & 10B (07/16), RF11A & 11B (07/17)	32.26% (10/31)
FASE	07/18 – 08/12/2016	16	RF6A, 6B, & 6C (07/29)	14.52% (9/62)
MACAWS	06/21 – 07/12/2018	16	RF12 (07/05), RF16 (07/12)	4.92% (3/61)
CSM	09/01 – 09/25/2020	14	RF1 (09/01), RF5 (09/09), RF6 (09/10)	13.33% (4/30)

149
150



151
 152 **Figure 1: Research flight paths for the six Twin Otter campaigns used in this study. The aircraft base at Marina, CA is**
 153 **denoted by a white diamond, and the IMPROVE station used in this study is indicated by a black star (Pt. Reyes National**
 154 **Seashore).**

155
 156 **2.1.1 Twin Otter Instrumentation**

157 Table 2 summarizes the relevant instruments used for each Twin Otter mission pertinent to this work. More
 158 extensive details about the instruments, and those not listed below such as relevant navigational and meteorological
 159 instruments, are described in Sorooshian et al. (2018).

160
 161 **Table 2: Summary of Twin Otter payload during the field campaigns used for this study. The six farthest right columns**
 162 **show instrument availability for each campaign.**



Instrument	Measured variable	Size range	Time resolution	E-PEACE	NiCE	BOAS	FASE	MACAWS	CSM
TSI Ultra-fine Condensation Particle Counter (CPC) 3025	$N_{a>3nm}$	$> 0.003 \mu m$	1 s	X	X	X	X	X	X
TSI Condensation Particle Counter (CPC) 3010	$N_{a>10nm}$	$> 0.01 \mu m$	1 s	X	X	X	X	X	X
PMS/DMT Passive Cavity Aerosol Spectrometer Probe (PCASP)	$N_{a0.1-1\mu m}$, $N_{a>1\mu m}$	$\sim 0.1 - 3.4 \mu m$	1 s	X	X	X	X	X	X
DMT Cloud and Aerosol Spectrometer - Forward Scattering (CASF)	N_d	$\sim 0.6 - 60 \mu m$	1 s	X	X		X	X	X
PMS/DMT Forward Scattering Spectrometer Probe (FSSP)	N_d	1 - 46 μm	1 s		X	X	X	X	
ARI Aerosol Mass Spectrometer (AMS)	Speciated mass conc.	$\sim 60 - 600 nm$	$< 15 s$	X	X	X			
Mohnen Cloud Water Collector - pH, IC, ICPMS	pH, air-equivalent mass conc.	N/A	$\sim 5 - 60 min$	X	X	X	X	X	

163

164

165

166

167

168

169

170

171

172

173

174

175

176

177

178

179

180

181

182

183

184

185

186

187

188

189

190

191

192

193

Condensation particle counters (CPCs; TSI, Inc.) were used to measure particle number concentrations for diameters greater than 3 ($N_{a>3nm}$ or N_{a3}) and 10 nm ($N_{a>10nm}$ or N_{a10}), respectively, as well as the Passive Cavity Aerosol Spectrometer Probe (PCASP; Particle Measuring Systems (PMS), Inc., modified by Droplet Measurement Technologies (DMT), Inc.) for diameters between ~ 100 nm and 3.4 μm . The Cloud and Aerosol Spectrometer – Forward Scattering (CASF; DMT, Inc.) measured the size distribution of larger particles and droplets between 0.6 – 60 μm for all missions except for BOAS when the Forward Scattering Spectrometer Probe (FSSP; PMS, Inc. modified by DMT, Inc.) was used in its place. The cloud probes were calibrated before each field campaign to ensure consistency between the instruments (Sorooshian et al., 2018). The CASF and FSSP size distributions were integrated to determine total N_d and liquid water content (LWC) when the aircraft was in cloud using the criterion of LWC needing to exceed 0.02 $g m^{-3}$; all instances of LWC less than 0.02 $g m^{-3}$ were considered cloud-free and only considered for quantification of aerosol variables such as total N_a in different size ranges (Fig. S1). Additionally, RFs categorized as southerly flow were filtered to only include data during periods when the horizontal wind direction was between 135° and 225°. A variety of statistics were calculated for the reported and derived variables (e.g., $N_{a>3nm}$, $N_{a>10nm}$, $N_{a10-100nm}$ ($N_{a>10nm} - N_{a0.1-1\mu m}$), $N_{a0.1-1\mu m}$, $N_{a>1\mu m}$, the ratio of N_{a3} to N_{a10} ($N_{a3}:N_{a10}$), N_d , horizontal wind speed and direction) in categories of interest including medians and minimum/maximum values. The mode was calculated for wind direction for each RF as well as each overall campaign, since that statistic is assumed here to be a better representation of typical wind directions rather than the median.

An Aerosol Mass Spectrometer (AMS; Aerodyne Research Inc. (ARI)) was used during some campaigns to measure sub-micrometer (submicron) aerosol composition, specifically for non-refractory components (SO_4^{2-} , NO_3^- , NH_4^+ , Cl⁻, and organics). Coggon et al. (2012; 2014) discuss in detail the AMS operational details and results from some of the campaigns. Cloud water (CW) was collected using a Mohnen CW collector, which was manually placed above the fuselage of the Twin Otter during cloud penetrations for sample collection into vials kept inside the aircraft. After flights, samples were analyzed for pH and speciated concentrations of various water-soluble ions and elements, with a number of studies summarizing the operational details and selected results (e.g., Wang et al., 2014; Wang et al., 2016; Macdonald et al., 2018). An Oakton Model 110 pH meter was used for E-PEACE, NiCE, and BOAS, and a Thermo Scientific Orion 8103BNUWP Ross Ultra Semi-Micro pH probe was used for FASE and MACAWS. Water-soluble ionic composition was measured via Ion Chromatography (IC; Thermo Scientific Dionex ICS – 2100 system), except some ions during E-PEACE, including Na^+ , could not be measured. Water-soluble elemental composition was measured via Inductively Coupled Plasma Mass Spectrometry (ICP-MS; Agilent 7700 Series) for E-PEACE, NiCE,



194 and BOAS, and via Triple Quadrupole Inductively Coupled Plasma Mass Spectrometry (ICP-QQQ; Agilent 8800
195 Series) for FASE and MACAWS. Cloud water was not collected during CSM. The IC species analyzed in this study
196 are Cl^- , NH_4^+ , NO_3^- , non-sea salt (nss)- SO_4^{2-} , and oxalate, and the ICPMS species analyzed are Ca^{2+} , K^+ , Na^+ , and V .
197 We used the following equation to calculate nss- SO_4^{2-} under the assumption that all Na^+ is from sea salt (e.g.,
198 AzadiAghdam et al., 2019):
199

$$200 \quad [nss - \text{SO}_4^{2-}] = [\text{SO}_4^{2-}] - 0.253 \times [\text{Na}^+] \quad (1)$$

201
202 Aqueous concentrations of ions and elements were converted into air-equivalent concentrations using the mean LWC
203 encountered when the aircraft was in cloud ($\text{LWC} > 0.02 \text{ g m}^{-3}$) during collection of individual samples.

204 Aircraft data were analyzed four different ways over the study domain. The primary focus of the analysis is
205 using data within the spatial domain listed in Sect. 2.1 only when the aircraft was over the ocean. In addition to a LWC
206 maximum of 0.02 g m^{-3} , another screening criterion was utilized to omit data during RFs strongly influenced by
207 wildfire emissions (Table 3), which was when the median flight-wide $N_{a>10\text{nm}}$ value exceeded $7,000 \text{ cm}^{-3}$ for altitudes
208 less than 800 m. This value was determined by closely examining flights that flew through areas with reported wildfire
209 influence using flight notes. Data were alternatively analyzed for RF segments only over the ocean without the $N_{a>10\text{nm}}$
210 criterion applied, and then also when the aircraft flew within the spatial domain over land and ocean both with and
211 without the same wildfire criterion; those results are shown in Tables S1 - S3. Note that CSM was the only campaign
212 for which this criterion was not applied, as smoke was the sole focus of the mission and the flights are considered to
213 all have been influenced to some extent. Moreover, CSM is unique amongst the campaigns examined where the
214 scientific hypotheses to be tested are not as applicable due to the widespread smoke coverage, but we still examine it
215 as it can provide useful insights.

216 Mann-Whitney U tests were performed for the aircraft data and the CW data, where the null hypotheses ($p \leq$
217 0.05) were that the medians of certain variables (N_a , N_d , wind speed and direction) and species concentrations of
218 southerly and northerly wind days were similar within a campaign.
219

220 2.2 Wind Direction Classification

221 To determine boundary layer wind direction in the study region, we used a number of data products, as each
222 provided unique advantages either related to temporal, spatial, or vertical coverage. Data from NOAA's National Data
223 Buoy Center (NDBC) were analyzed to verify the ocean surface wind direction was between 135° and 225° , which is
224 considered southerly in this study. We focused on wind direction during 1400 - 2200 UTC to overlap with when the
225 majority of RFs occurred (Marina, CA is 7 hours behind UTC). Other days classified as northerly flow adhered to
226 surface wind direction between 315° and 45° . Five buoys were used to match the ones used in Juliano et al. (2019a):
227 46011 (Santa Maria: 34.94° N , 120.99° W), 46013 (Bodega Bay: 38.24° N , 123.32° W), 46014 (Point Arena: 39.23°
228 N , 123.98° W), 46028 (Cape San Martin: 35.77° N , 121.90° W), and 46042 (Monterey: 36.79° N , 122.40° W). Buoy
229 locations relative to the CA coast are shown in Fig. 1 of Juliano et al. (2019a).

230 We used Multi-Channel RGB data from the Geostationary Operational Environmental Satellite-WEST Full Disk
231 Cloud Product (GOES-15) at time resolutions of every three hours for E-PEACE, hourly for NiCE, BOAS, FASE,
232 and MACAWS, and every half-hour for CSM. Wind direction was assessed via cloud movement, which was partly a
233 focus of this study (e.g., boundary layer cloud characteristics) with particular attention paid to the principal RF time
234 period. We investigated all days within a campaign month, and not just days coinciding with a RF. For example, E-
235 PEACE comprised flights from 9 July to 18 August 2011, and thus GOES data from 1 July through 31 August 2011
236 were investigated for that year.

237 The National Oceanic and Atmospheric Administration (NOAA) Hybrid Single-Particle Lagrangian Integrated
238 Trajectory (HYSPLIT; Stein et al., 2015; Rolph et al., 2017) model was also used to obtain back trajectories based on
239 North American Mesoscale Forecast System (NAM) meteorological data (12 km resolution) ending at 36.67° N ,
240 121.60° W for 500, 900, 2,500, and 4,500 m AGL. These altitudes were selected to both capture marine boundary
241 layer (MBL) and free troposphere (FT) winds and reflect the variety of altitudes the Twin Otter aircraft flew at during
242 the six campaigns in Table 1; however, the trajectories at 500 m were most important for connecting to the aircraft
243 data analysis.

244 For Twin Otter flight days, aircraft wind data were used to confirm that wind direction was either southerly or
245 northerly in the lowest 800 m of the flights (over ocean and land), which was the altitude range of most of the flight



246 time. For a case-by-case basis, archived surface weather charts were accessed via the NOAA Weather Prediction
247 Center (WPC) to investigate wind direction at specific sites (like Pt. Reyes).

248

249 **2.3 NAAPS and COAMPS**

250 Both the Navy Aerosol Analysis and Prediction System (NAAPS; Lynch et al., 2016;
251 <https://www.nrlmry.navy.mil/aerosol/>) and the Coupled Ocean/Atmosphere Mesoscale Prediction System (COAMPS;
252 Hodur, 1997) are used to support the analysis of airborne data collected during the six Twin Otter campaigns and
253 assess how well they can simulate southerly flow on days when observational datasets indicate such flow directions
254 offshore of CA. NAAPS is a global aerosol forecast model run by the U.S. Naval Research Laboratory (NRL) in
255 Monterey, CA that predicts 3-dimensional anthropogenic and biogenic fine (ABF), dust, sea salt, and biomass burning
256 smoke particle concentrations in the atmosphere. NAAPS relies on meteorological data derived from the Navy Global
257 Environmental Model (NAVGEM; Hogan et al., 2014) and considers 25 vertical levels in the troposphere. For this
258 study, we utilized the reanalysis version of NAAPS (NAAPS-RA, hereafter called NAAPS) that assimilates aerosol
259 depth observations to get a general sense of the simulated differences between southerly and northerly flow days for
260 our region of focus and as a complement to the aircraft data. We investigated data for northward wind speed (v_{wind})
261 and mass concentrations for ABF aerosols and sea salt (Fig. 2), along with smoke, dust, coarse aerosol, and fine aerosol
262 (Fig. S2). Note that ABF represents secondarily formed species (SO_4^{2-} and secondary organic aerosol) and primary
263 organic aerosol generally within the fine mode ($<1 \mu m$). To approximate the average boundary layer height of all the
264 missions used in this study, the first five vertical levels (max height of ~ 668 m above sea level) of NAAPS were used
265 for data analysis.

266 For our analysis, the NAAPS data were first separated into southerly and northerly flow days for each campaign
267 based on results from Sect. 2.2, and the average value of each parameter was calculated for four reported times: 0000,
268 0600, 1200, and 1800 UTC. The most focus is placed on 1800 UTC, as that time coincided with most Twin Otter
269 flight periods (results for the remaining time periods are in Fig. S3-S9). Then, all the parameters except v_{wind} were
270 summed across the five vertical levels to get a total mass concentration ($\mu g m^{-3}$) up to ~ 668 m above sea level, whereas
271 the average was calculated for v_{wind} . Those values were used to calculate the difference between southerly and
272 northerly flow days at $1.0^\circ \times 1.0^\circ$ spatial resolution.

273 COAMPS is a high-resolution meteorological forecast model developed by the NRL's Marine Meteorology
274 Division (MMD) that outputs parameters like air temperature, winds, precipitation, cloud base and top heights, and
275 mass concentrations for the same aerosol species as those in NAAPS. For this study, we assessed the wind
276 speed/direction and smoke from COAMPS and NAAPS for the purpose of contrasting with observational data.
277 COAMPS maps were generated for this study by NRL at three different resolutions: 45 km, 15 km, and 5 km. To
278 compare to NAAPS, 15 km resolution grids were used. To assess the efficacy of COAMPS and NAAPS at forecasting
279 heavy pollution on a day with southerly winds, we performed a comparison of the two models for CSM RF 6 at 1800
280 UTC to match the flight time. The focus areas for both COAMPS and NAAPS matched that of the aircraft data
281 mentioned in Sect. 2.1.1. The altitudes used for the COAMPS maps for wind speed/direction and smoke were 762 m
282 and 305 m, respectively, as the best match to the NAAPS maximum altitude used in this work.

283

284 **2.4 IMPROVE**

285 To investigate the difference in surface-level aerosol measurements between southerly and northerly flow days,
286 this study utilized composition data from the Interagency Monitoring of Protected Visual Environments (IMPROVE)
287 network (Malm et al., 1994; <http://views.cira.colostate.edu/fed/>). Data were taken from the Pt. Reyes National
288 Seashore surface station ($38.07^\circ N$, $122.88^\circ W$) for the full campaign months shown in Table 1. Every third day,
289 gravimetric mass of particulate matter ($PM_{2.5}$ and PM_{10}) was measured. The $PM_{2.5}$ fraction was further analyzed via
290 ion chromatography and X-ray fluorescence (XRF) for water-soluble ions and elements, respectively, along with
291 organic and elemental carbon (OC and EC).

292 This study specifically investigated ($\mu g m^{-3}$): $PM_{2.5}$, coarse mass ($PM_{coarse} = PM_{10} - PM_{2.5}$), Cl⁻, NO₃⁻, SO₄²⁻, Ni,
293 K⁺, Si, V, EC, OC, and fine soil. The total OC measurement comes from a summation of four fractions of OC, which
294 are categorized by a method of carbon analysis detection temperature (e.g., Chow et al., 1993; Watson et al., 1994).
295 This method quantifies methane produced via volatilization of particulate species in pure helium at 120°C (OC1),
296 250°C (OC2), 450°C (OC3), and 550°C (OC4). Similarly, the total EC measurement is a summation of three fractions



297 categorized via combustion temperatures in a 98% pure helium and 2% pure oxygen environment: 550°C (EC1),
298 700°C (EC2), and 800°C (EC3). Fine soil concentrations are calculated as follows (Malm et al., 1994):

299
300
$$\text{Fine soil } (\mu\text{g m}^{-3}) = 2.2 \times [Al] + 2.49 \times [Si] + 1.63 \times [Ca] + 2.42 \times [Fe] + 1.94 \times [Ti] \quad (2)$$

301

302 This equation was confirmed by several studies (e.g., Cahill et al., 1981; Pitchford et al., 1981; Malm et al., 1994)
303 through comparisons of resuspended soils and ambient particles.

304 Upon examination, it was decided to only use data for E-PEACE and BOAS because those campaign periods
305 had more than a single point with valid data for southerly days (three and two, respectively); recall that IMPROVE
306 data are only available every third day so some southerly days would not necessarily have available IMPROVE data.
307 All the species analyzed had a status flag of “V0” (“Valid value”) or “V6” (“Valid value but qualified due to non-
308 standard sampling conditions”), which are both considered valid data. We chose to include data flagged as “V6” (Cl⁻,
309 NO₃⁻, and SO₄²⁻ for BOAS) due to the small quantity of usable data for southerly days. Additional information, like
310 sampling protocols, are provided elsewhere (<http://vista.cira.colostate.edu/Improve/sops/>). Like the aircraft and CW
311 data, Mann-Whitney U tests were performed on this dataset to determine if the median species concentrations were
312 equivalent for southerly and northerly days across a campaign.

313

314 2.5 MODIS

315 To assess cloud characteristics of southerly and northerly flow days during the campaign months of this study,
316 we retrieved daily mean values within the same focus region defined for aircraft data in Sect. 2.1.1 (35.31° N – 40.99°
317 N, 125.93° W – 118.98° W) for the following properties from the MODerate resolution Imaging Spectroradiometer
318 (MODIS) on Aqua through NASA Giovanni (<https://giovanni.gsfc.nasa.gov/giovanni/>): cloud effective particle radius
319 (r_e ; μm), cloud liquid water path (LWP; g m^{-2}), cloud optical thickness (COT), cloud fraction (from cloud mask), and
320 aerosol optical depth (AOD, combined dark target and deep blue at 0.55 μm for land and ocean). N_d (cm^{-3}) was
321 calculated from MODIS properties based on the following equation (Painemal and Zuidema, 2011):

322
$$N_d = 1.4067 \times 10^{-6} [cm^{-0.5}] \times \frac{COT^{0.5}}{r_e^{2.5}} \quad (3)$$

323 Additionally, retrieval data were only used when cloud fraction $\geq 30\%$ to maximize both data reliability and sample
324 size (Mardi et al., 2021). The focus of the analysis is comparing median values of these remotely sensed variables
325 between southerly and northerly days for E-PEACE and BOAS due to a similar LWP value for the two flow regimes
326 (66.48/67.17 g m^{-2} and 84.40/89.90 g m^{-2} , respectively). Data for the other campaigns are included in the SI.
327 Additionally, this study used MODIS visible imagery on NASA Worldview to qualitatively identify smoke plumes,
328 in addition to fire radiative power from the MODIS Fire Information for Resource Management System (FIRMS;
329 <https://earthdata.nasa.gov/firms>).

330

331 3 Results and Discussion

332 3.1 Lower Tropospheric Wind Profile

333 We first examine NAAPS and airborne observations for the lower tropospheric wind profile during the
334 periods of analysis shown in Table 1. Note that the other datasets described in Sect. 2.2 are consistent with the airborne
335 wind results and thus only NAAPS and aircraft data are discussed here for two reasons: NAAPS results are used to
336 assess how such a model quantifies differences in winds between southerly and northerly flow days as identified with
337 methods in Sect. 2.2, whereas aircraft data provide insight into typical wind speeds during southerly and northerly
338 flow periods.

339 Beginning with the aircraft data, results are discussed here only for measurements over the ocean with the
340 $N_{a>10nm}$ filter applied to remove smoke influence (Table 3). The mode of wind directions during southerly and northerly
341 flow days in each campaign expectedly aligned with southerly (144° – 194°) and northerly flow (327° – 332°),
342 respectively, because of how the classification was done (Sect. 2.2). Median wind speeds across each campaign ranged
343 from 2.35 – 7.75 m s^{-1} for southerly flow in contrast to 5.12 – 8.87 m s^{-1} for northerly flow. This finding differs from
344 what has been observed in previous studies, likely due to the difference in sampling location: aircraft observations
345 from the surface to 800 m versus buoy/surface observations, respectively. All campaigns featured higher median wind
346 speeds for northerly flow flights. Both the median wind speeds and directions of southerly and northerly days were
347 significantly distinct from one another for all of the studied campaigns (Table S4).



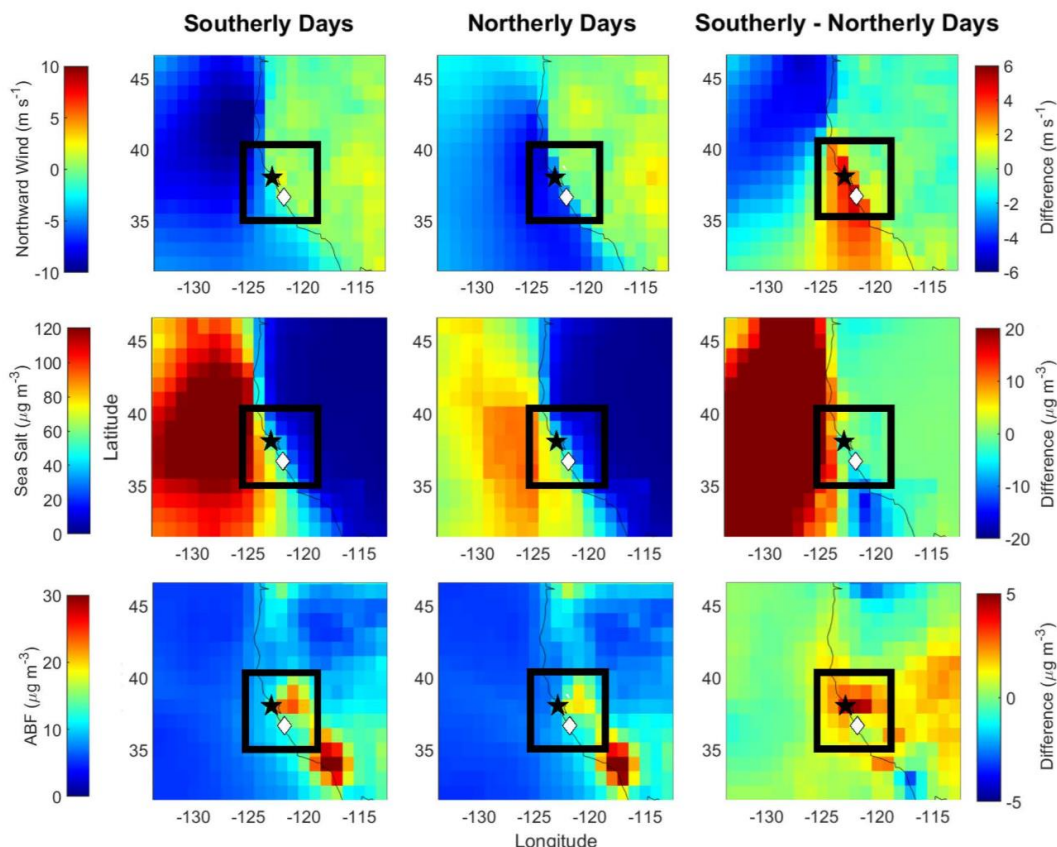
348
 349
 350
 351
 352
 353
 354
 355
 356

Table 3: Median values (southerly/northerly) of various parameters over the ocean with an $N_{a>10nm}$ filter such that RFs with median $N_{a>10nm} > 7,000 \text{ cm}^{-3}$ were removed from the final analysis to eliminate smoke interference. Mode values are used for wind direction. The instruments used for the parameters from left to right are as follows: CPC 3010, CPC 3010 – PCASP $<1\mu\text{m}$, PCASP $<1\mu\text{m}$, PCASP $>1\mu\text{m}$, CPC 3025/CPC 3010, CASF. The far right-hand columns indicate the number of datapoints used from each campaign, with n_{Na} indicating the amount of data used for all N_a calculations, n_{Nd} is for cloud data, and n_{wind} is for wind speed and direction. FSSP data were used for N_d data only during BOAS, whereas CASF was used in other campaigns. These data are for the lowest 800 m above sea level. The reader is referred to Fig. S10 for box plots corresponding to the analysis in this table, as well as Table S4 for Mann-Whitney U p-values.

	$N_{a>10nm}$ (cm^{-3})	$N_{a10-100nm}$ (cm^{-3})	$N_{a0.1-1\mu\text{m}}$ (cm^{-3})	$N_{a>1\mu\text{m}}$ (cm^{-3})	$N_{a3-N_{a10}}$ (-)	N_d (cm^{-3})	Wind Speed (m s^{-1})	Wind Direction ($^\circ$)	n_{Na} ($\times 10^3$)	n_{Nd} ($\times 10^3$)	n_{wind} ($\times 10^3$)
E-PEACE	861 / 703	501 / 454	338 / 197	0 / 1.25	1.09 / 1.10	252 / 163	3.38 / 7.58	177.61 / 330.48	20.3 / 202.7	17.1 / 127.1	37.4 / 330.8
NICE	953 / 606	248 / 245	471 / 260	2.51 / 0	1.12 / 1.17	249 / 254	3.80 / 5.12	180.81 / 327.20	1.4 / 66.8	1.5 / 39.6	3.0 / 112.8
BOAS	750 / 497	553 / 256	204 / 196	0 / 1.24	1.20 / 1.18	143 / 127	5.49 / 6.35	166.97 / 328.58	5.8 / 72.1	3.9 / 20.5	11.8 / 104.7
FASE	836 / 916	423 / 635	326 / 180	0 / 0	1.29 / 1.16	203 / 223	2.35 / 6.82	144.03 / 331.29	1.0 / 95.5	0.3 / 99.2	1.3 / 194.9
MACAWS	722 / 815	560 / 635	154 / 164	0 / 0	1.25 / 1.26	189 / 165	7.75 / 8.87	162.15 / 330.28	10.3 / 118.9	6.6 / 27.0	16.9 / 145.9
CSM	5,558 / 3,451	5,081 / 3,366	515 / 365	1.00 / 0	1.30 / 1.67	334 / 314	6.10 / 6.77	193.93 / 332.16	4.8 / 31.5	1.8 / 4.1	6.9 / 41.3

357
 358
 359
 360
 361
 362
 363
 364
 365
 366
 367
 368
 369
 370
 371
 372
 373
 374
 375

NAAPS values are discussed for v_{wind} for the lowest ~668 m above sea level, with positive (negative) values representing southerly (northerly) flow (Fig. 2). This altitude range coincides with the airborne data shown in Table 3. The v_{wind} data are categorized into “Southerly Days,” “Northerly Days,” and “Southerly – Northerly Days” for 1800 UTC, which overlaps with most of the Twin Otter flight times (Fig. 1); results for 0000, 0600 and 1200 UTC are provided in Fig. S3. Both southerly and northerly days had less negative v_{wind} closer to the coast (up to 35° N) compared to farther offshore over the ocean ($\sim -3/-9$ and $-4/-6 \text{ m s}^{-1}$, respectively, for southerly/northerly flow). Slower, slightly northerly winds extended farther north to Marina and west to 123.5° W for southerly days, which is illustrated in red (differences exceeding $\sim 3 \text{ m s}^{-1}$ between flow regimes) in the “Southerly – Northerly Days” panel. Northerly days also had an area of less negative v_{wind} north of 43.5° N , which is emphasized in the “Southerly – Northerly Days” panel in blue (differences of $-4 - -6 \text{ m s}^{-1}$). NAAPS was not able to fully capture southerly winds over the ocean and along the coast in that v_{wind} was not clearly positive; however, the magnitude of the wind speed difference along the coastal area of the study domain appeared to align with the mechanics of coastal wind reversal and CTDs: the weakening of northerly wind and ultimate reversal of flow (e.g., Winant et al., 1987; Melton et al., 2009). A key conclusion from NAAPS is that the difference between southerly and northerly flow days matches expectations with southerly days having at least a greater tendency towards more positive v_{wind} but still not necessarily distinctly positive.



376
 377 **Figure 2:** Average northward wind speed (v_{wind} ; $m s^{-1}$), total sea salt mass concentration ($\mu g m^{-3}$), and total ABF mass
 378 concentration ($\mu g m^{-3}$) of campaign months at 1800 UTC for 1st through 5th NAAPS levels (up to ~668 m above sea level)
 379 for southerly and northerly flow wind days. The right-most panel illustrates the difference between southerly and northerly
 380 flow days. The airbase in Marina, CA is denoted by a white diamond, Pt. Reyes is indicated with a black star, and the black
 381 box indicates the region of focus in this study.

382
 383 **3.2 Aerosol Response to Southerly Flow**

384 **3.2.1 Fire Radiative Power Maps**

385 Prior to discussing aerosol results, we address the influence of wildfire emissions, which is an aerosol source
 386 that varies in terms of strength between the six campaign periods in contrast to shipping and other forms of continental
 387 emissions that are more consistent year to year. Past studies using airborne and surface-based data at Marina
 388 overlapping with the six campaigns in Table 1 revealed the following in terms of notable biomass burning influence
 389 around Marina and offshore areas (e.g., Prabhakar et al., 2014; Braun et al., 2017; Mardi et al., 2018): (i) E-
 390 PEACE/BOAS: no major influence of note; (ii) NiCE: influence around the last week of July 2013; (iii) FASE:
 391 influence between 25 July and 12 August; (iv) MACAWS: significant influence on flights during 28 June and 3 July
 392 owing to the aircraft having flown close to wildfire areas inland in northern CA; (v) CSM: significant influence
 393 throughout the campaign. These archived notes do not preclude the possibility of biomass burning influence during
 394 other periods of those campaigns as it relates to Twin Otter aerosol and cloud measurements.

395 Spatial maps of fire radiative power (FRP; Fig. 3), indicative of burn intensity, show relatively less burning
 396 activity in immediate proximity to Marina during E-PEACE and BOAS. In contrast, the other campaigns show clusters
 397 of burning spots around Marina. Note that CSM, by virtue of its name, was focused largely on wildfires with dedicated
 398 RFs to sample smoke. MACAWS also was designed as a wildfire study but had less cases of strong plumes to sample,



399 which included RFs on 28-29 June farther inland than most RFs, resulting in very high aerosol number concentrations
400 ($N_{a>10nm} > 10,000 \text{ cm}^{-3}$).

401

402 **3.2.2 Fine Aerosol**

403 The first hypothesis of this study is that southerly flow yields higher fine aerosol levels associated with
404 anthropogenic and continental tracer species due to more perceived influence from land and shipping sources (Juliano
405 et al., 2019a; 2019b). This was also speculated by Hegg et al. (2008) although it was not examined in great detail by
406 that study. Here we rely on results from a number of datasets including measurements from the Twin Otter (Tables 3
407 and 4) and the Pt. Reyes IMPROVE site (Fig. 4), along with NAAPS model results (Fig. 2).

408

409 **3.2.2.1 Airborne: Particle Concentration**

410 Beginning with the Twin Otter data, aerosol data for 17 southerly flight days corresponding to 21 RFs were
411 compared to 93 other flight days with predominantly northerly flow in Table 3 (box plots of the variables in Fig. S10,
412 and Mann-Whitney U test results are in Table S4), as well as Tables S1-S3. We focus primarily on flight data over the
413 ocean with the $N_{a>10nm}$ filter applied to omit wildfire influence; the other aircraft data result tables in the Supplement
414 generally show the same trends as Table 3. We caution that the results of FASE, and to a slightly lesser extent NiCE,
415 are not as meaningful as the other campaigns owing to the least amount of statistics for southerly conditions, with
416 numbers of datapoints shown in the tables.

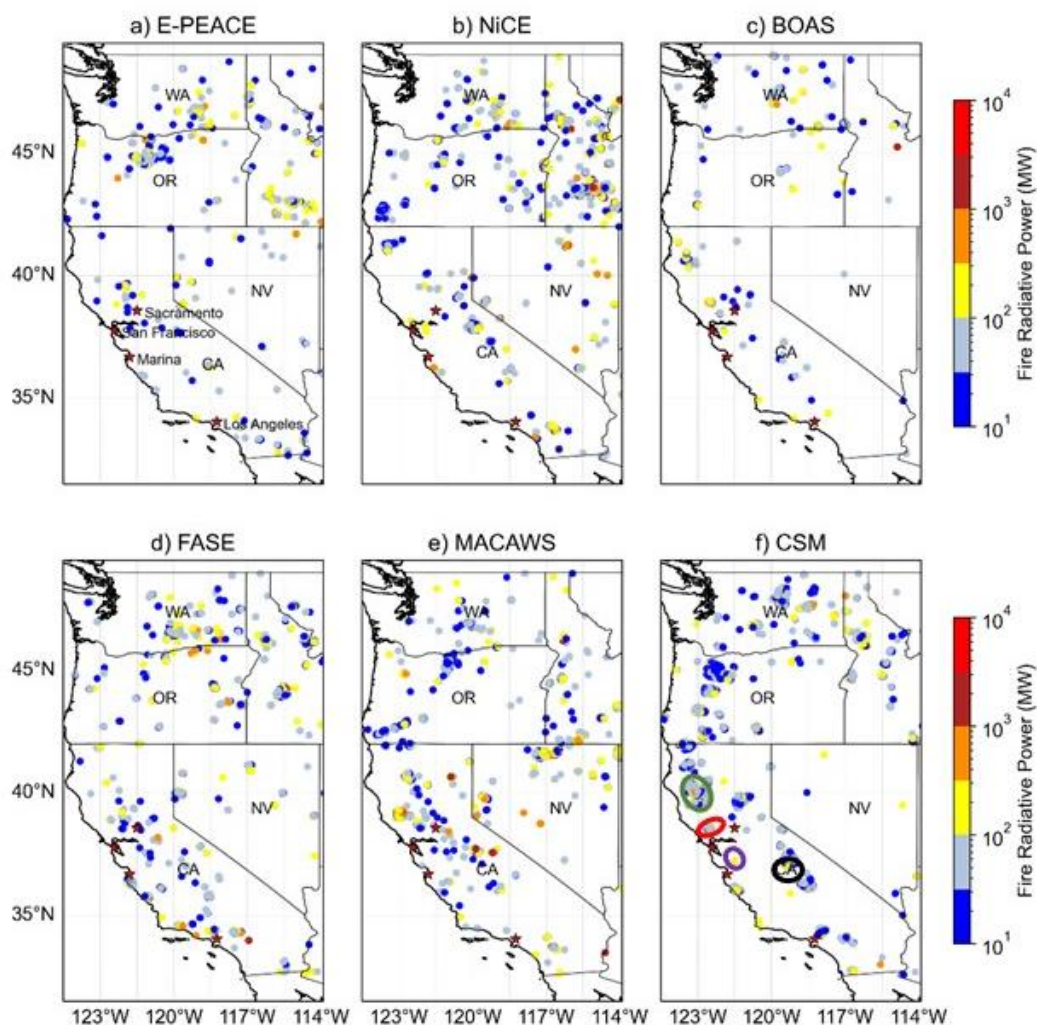
417

418 The total submicron aerosol number concentration, $N_{a>10nm}$, was far larger for southerly flow ($722\text{-}5,558 \text{ cm}^{-3}$)
419 as compared to northerly flow flights ($497\text{-}3,451 \text{ cm}^{-3}$). Of the six campaigns, the only ones with higher median
420 values in northerly flow were FASE and MACAWS, with small $\Delta N_{a>10nm}$ of -80 cm^{-3} and -93 cm^{-3} , respectively. CSM
421 exhibited the largest difference in median values for $N_{a>10nm}$ between southerly and northerly flow ($\Delta N_{a>10nm} = 2,107$
422 cm^{-3}), followed by NiCE ($\Delta N_{a>10nm} = 347 \text{ cm}^{-3}$) and BOAS ($\Delta N_{a>10nm} = 253 \text{ cm}^{-3}$). While these campaigns have a
423 smaller relative sample size of southerly data ($n_{Na} < 6 \times 10^3$; CSM: 4.8×10^3 , NiCE: 1.4×10^3 ; and BOAS: 5.8×10^3), E-
424 PEACE has a sizable amount of southerly data (20.3×10^3) and the least fire influence of the missions included in this
425 study, so we find it may be the most reliable campaign to analyze. There was a distinct difference between southerly
426 and northerly days during E-PEACE as well, with a $\Delta N_{a>10nm}$ of 158 cm^{-3} . As the number concentration in the
427 submicron range dominates the total CPC concentrations, these results convincingly point to an enhancement of fine
428 aerosol pollution in southerly flow even without the $N_{a>10nm}$ filter (Table S1).

429

430 We examined various size ranges of particles in the submicron range as well. For particles between 10-100
431 nm, southerly conditions generally had higher number concentrations except again for FASE and MACAWS and with
432 more comparable levels during NiCE. As particles larger than 100 nm are more relevant for cloud condensation nuclei
433 (CCN) activity, we also examined number concentrations for diameters between 0.1 and $1 \mu\text{m}$, which show higher
434 southerly levels except for MACAWS. Between campaigns, CSM overall exhibited the highest particle concentrations
435 in this size range due to extensive wildfire emissions in the area, which are known to be linked with enhanced levels
436 of particles larger than 100 nm in the same region (Mardi et al., 2018), which is why this campaign shows relatively
437 large PCASP enhancements in both southerly and northerly flow conditions relative to the other campaigns (see in
438 particular Tables S1-S2). Without the CPC filter (Table S1), only the medians for NiCE and BOAS on northerly wind
439 days changed, resulting in the $N_{a10-100nm}$ median during NiCE to be lower during southerly flow days compared to
440 northerly days. When looking within the region of focus, the inclusion of land data in addition to ocean data (Tables
441 S2-S3) leads to significant N_a differences (to a lesser extent for the filtered data, Table S3) compared to Table 3,
including higher submicron concentrations for NiCE, BOAS, and FASE.

441



442
443 **Figure 3: Spatial maps of fire radiative power (FRP), downloaded from the MODIS Fire Information for Resource**
444 **Management System (FIRMS; <https://earthdata.nasa.gov/firms>) for the entire months spanning individual field**
445 **campaigns in Table 1. Only FRP values with a high detection confidence level ($\geq 80\%$) are shown (Giglio et al., 2015). The**
446 **circled areas in panel (f) correspond to some of the largest wildfires in CA state history that occurred in 2020 that are**
447 **referred to in Sect. 3.4.2: August Complex fire (green), SCU Lightning Fire Complex (purple), Creek fire (black), and**
448 **LNU Lightning Complex fire (red).**

449
450 Although new particle formation (NPF) was not expected to be prominent in the lower 800 m owing mostly
451 to high aerosol surface areas especially due to sea spray emissions, we still examined the ratio of N_a above 3 nm
452 relative to 10 nm ($N_{a3}:N_{a10}$), as this ratio is a commonly used marker for identifying NPF. Such instances are more
453 common in the free troposphere in the study region owing to reduced aerosol surface areas (Dadashazar et al., 2019).
454 The results suggest that the $N_{a3}:N_{a10}$ ratios for the two flow regimes were significantly different for all the campaigns
455 except for MACAWS (higher ratios in southerly flow for BOAS and FASE), with median flow direction-dependent



456 values per campaign ranging from 1.09 to 1.30. During CSM, the median ratio value was 1.67 in northerly flow
 457 conditions due to presumed influence from high precursor levels in smoke plumes.

458

459 **3.2.2.2 Airborne: Tracer Species in Cloud Water**

460 We next turn to CW composition data (Table 4) to continue learning more about the effect of southerly flow
 461 and its associated emission sources. NiCE and FASE were not included in the CW calculations of Table 4 (but shown
 462 in Fig. S11) because there were fewer than five samples from RFs with southerly wind direction for those two
 463 campaigns, and CW was not collected during CSM. NO_3^- and nss-SO_4^{2-} , both representative of fine aerosol pollution,
 464 were higher for southerly days, with a significant difference (Table S5) apparent in E-PEACE (1.80/0.30 and 2.10/0.81
 465 $\mu\text{g m}^{-3}$ for southerly and northerly days, respectively), as well as for NO_3^- during BOAS (1.02/0.23 $\mu\text{g m}^{-3}$ for southerly
 466 and northerly days, respectively). The same trend was observed for V (ship exhaust tracer) and NH_4^+ , which can be
 467 used as a tracer for continental sources such as agriculture (Juliano et al., 2019b). Thus, these results help to provide
 468 more confidence in results from Juliano et al. (2019b) but with increased statistics across more campaigns. For E-
 469 PEACE and MACAWS, there were also lower southerly flow concentrations of K^+ (0.01/0.05 and 0.06/0.11 $\mu\text{g m}^{-3}$)
 470 and Ca^{2+} (0.05/0.07 and 0.06/0.16 $\mu\text{g m}^{-3}$), suggestive of less influence from biomass burning and dust sources with
 471 the caveat that K^+ and Ca^{2+} have sources other than biomass burning and dust.

472 There were also higher concentrations of oxalate during southerly days, which can be used as a tracer for aqueous
 473 processing (Hilario et al., 2021), wherein cloud droplets are formed from oxidized volatile organic compounds (Ervens
 474 et al., 2011; Ervens, 2015; McNeill, 2015). Further, there were significant differences in median concentrations
 475 between southerly and northerly flow days during BOAS and MACAWS (0.12/0.05 and 0.08/0.03 $\mu\text{g m}^{-3}$,
 476 respectively). Precursors to oxalate are diverse including from biogenic sources, biomass burning, combustion (e.g.,
 477 Stahl et al., 2020 and references therein), shipping, along with being associated with sea salt and dust owing to gas-
 478 particle partitioning (Sorooshian et al., 2013; Stahl et al., 2020; Hilario et al., 2021); such sources are presumed to be
 479 influential during southerly flow based on the notion that air masses are influenced by some combination of continental
 480 emissions and extended time in shipping lanes.

481 Cloud water pH was lower and thus more acidic on southerly days for all three campaigns (3.85/4.54, 4.30/4.34,
 482 4.33/4.62 for southerly/northerly days during E-PEACE, BOAS, and MACAWS, respectively, and statistically
 483 different for E-PEACE and BOAS), which is another indicator for anthropogenic pollution enriched with acidic
 484 species (Pye et al., 2020). Increased acid levels can result in more Cl^- depletion when considering sea salt particles
 485 (e.g., Edwards et al., 2023 and references therein); interestingly, southerly days were characterized by lower $\text{Cl}^-:\text{Na}^+$
 486 ratios with median values of 1.39 (MACAWS), 1.63 (E-PEACE) (both campaigns of which southerly days were
 487 significantly different from northerly flow days), and 2.48 (BOAS), although the difference in MACAWS was only
 488 0.12. Braun et al. (2017) noted that, theoretically, over 60% of the Cl^- depletion in the submicron range could be
 489 attributed to nss-SO_4^{2-} , and greater than 20% in the supermicron range could be attributed to NO_3^- . As was noted
 490 previously, nss-SO_4^{2-} and NO_3^- were noticeably enhanced during southerly flow days while the $\text{Cl}^-:\text{Na}^+$ ratios were
 491 reduced. Schlosser et al. (2017) also reported that organic acids, notably oxalate, were significantly enhanced during
 492 periods of Cl^- depletion, which is reflected in our CW data. As E-PEACE was statistically the most robust dataset (and
 493 all CW species except Ca^{2+} , NH_4^+ , and oxalate had medians that were significantly different between southerly and
 494 northerly flow days), the results from CW convincingly align with more shipping and/or continental influence in
 495 southerly flow to impact cloud composition.

496

497 **Table 4: Median values (southerly/northerly) of water-soluble CW composition ($\mu\text{g m}^{-3}$) over the entirety of three**
 498 **campaigns with sufficient data. The starred (*) values are reported in ng m^{-3} . The number of samples used in each campaign**
 499 **is in the far-right hand column (n). The reader is referred to Table S5 which shows the p-values from the Mann-Whitney**
 500 **U tests, as well as Fig. S11 which shows box plots of the CW composition results for the five campaigns with available data.**
 501 **Values shown as “-” denote when samples were below the limit of detection.**

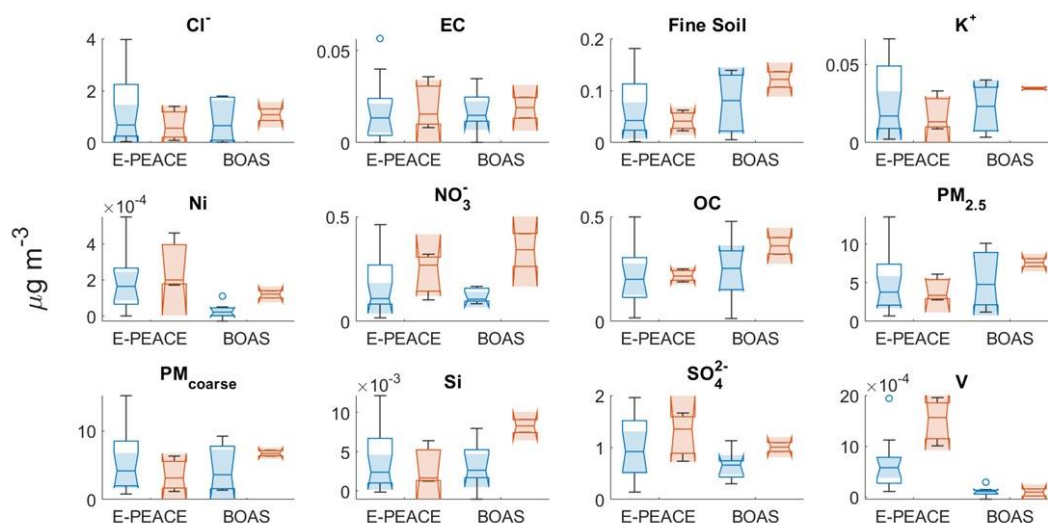
	Ca^{2+}	Cl^-/Na^+	K^+	Na^+	NH_4^+	NO_3^-	Oxalate	pH	nss-SO_4^{2-}	V	n
E-PEACE	0.05/0.07	1.63/2.15	0.01/0.05	0.42/1.21	— / —	1.80/0.30	0.02/0.02	3.85/4.54	2.10/0.81	2.16*/0.38*	10/65
BOAS	0.11/0.08	2.48/2.74	0.06/0.06	1.99/1.55	0.44/0.04	1.02/0.23	0.12/0.05	4.30/4.34	1.08/0.83	—/0.15*	5/21
MACAWS	0.06/0.16	1.39/1.51	0.06/0.11	1.30/2.70	0.08/0.05	0.55/0.38	0.08/0.03	4.33/4.62	0.56/0.26	0.07*/0.05*	15/51

502
 503



504 **3.2.2.3 Surface: Aerosol Composition**

505 We next examine surface composition data from the Pt. Reyes IMPROVE site. Mass concentrations of twelve
 506 PM composition variables were investigated to analyze important tracers along the coast (Fig. 4), with Mann-Whitney
 507 U test p-values for comparing southerly and northerly flow days shown in Table S6. It is important to recall that E-
 508 PEACE and BOAS were the only campaigns that had more than a single day of valid data coinciding with southerly
 509 flow because of the added challenge of IMPROVE sampling occurring every third day; therefore, northerly days had
 510 significantly more data points (18 for E-PEACE and seven for BOAS) compared to southerly days (three and two,
 511 respectively). That is the general reason for the large whiskers on the box plots for northerly RFs during E-PEACE
 512 and the lack of whiskers for southerly RFs during BOAS. Another feature to note is the ‘folded over’ appearance of
 513 some of the box plots. This indicates a high variance within the dataset and a skewed distribution. We caution that this
 514 analysis is not very statistically robust owing to the rare nature of southerly days in overlap with IMPROVE sampling;
 515 however, we take a ‘better than nothing’ approach to use in a supportive role in comparison to other datasets used to
 516 assess differences between southerly and northerly flow.
 517



518 **Figure 4: Box plots of IMPROVE data from the Pt. Reyes surface station. The southerly data for E-PEACE and BOAS**
 519 **(three and two points, respectively) are represented by the red boxes, and the northerly data (18 and seven, respectively)**
 520 **are represented by the blue boxes.**
 521
 522

523 SO_4^{2-} , NO_3^- , OC, V, Ni, and EC are reasonable tracer species representative of either shipping and/or continental
 524 sources in the study region (Wang et al., 2014; Maudlin et al., 2015; Wang et al., 2016; Dadashazar et al., 2019; Ma
 525 et al., 2019) hypothesized to be more enhanced in the coastal CA zone on southerly flow days due to air spending time
 526 over shipping lanes and land upwind of the study region. Even with the limited southerly flow statistics, the results of
 527 Fig. 4 support this idea as southerly conditions coincide with higher median concentrations of these species than
 528 northerly days. The most striking relative differences were for NO_3^- (southerly/northerly): 0.27/0.11 and 0.34/0.10 μg
 529 m^{-3} for E-PEACE and BOAS, respectively. NO_3^- was the only species during BOAS that was found to have a median
 530 concentration that was statistically different between southerly and northerly days (Table S6). Ni and V are the primary
 531 trace metals in heavy ship fuel oils and are commonly used as tracers for ship emissions (Celo et al., 2015; Corbin et
 532 al., 2018), and V was previously found enhanced in CW linked to ship emissions in E-PEACE (Coggon et al., 2012;
 533 Prabhakar et al., 2014). There were mostly higher concentrations of these species on southerly flow days (E-PEACE
 534 southerly/northerly: 0.20/0.17 and 1.56/0.58 ng m^{-3} , respectively; BOAS southerly/northerly: 0.12/0.02 and 0.09/0.11
 535 ng m^{-3} , respectively), supporting the hypothesis of elevated shipping emissions. Also, a Mann-Whitney U test found
 536 that the median V concentrations during E-PEACE were statistically different for southerly and northerly days (Table
 537 S6).



538 Only BOAS exhibited higher $PM_{2.5}$ during southerly days compared to northerly days ($7.61/4.82 \mu\text{g m}^{-3}$,
539 respectively), with E-PEACE having roughly equivalent concentrations for the two flow regimes ($3.39/3.78 \mu\text{g m}^{-3}$,
540 respectively). This is likely owing to how $PM_{2.5}$ is not the best marker for shipping and continental emissions owing
541 to its inclusion of other species of marine and natural origin.

543 3.2.2.4 NAAPS: Aerosol Composition

544 To round out discussion of fine aerosol pollution, we discuss NAAPS model results (Fig. 2). The largest
545 enhancements in ABF mass concentrations occurred inland both north of Marina around Pt. Reyes and near the Ports
546 of Los Angeles and Long Beach. There was $>5 \mu\text{g m}^{-3}$ difference in ABF concentration between southerly and
547 northerly days near Pt. Reyes. This suggests that while there were elevated levels of anthropogenic emissions in this
548 area regardless of the flow regime, there were increased concentrations during southerly flow days according to
549 NAAPS. Additionally, there is a strong ABF signal ($>30 \mu\text{g m}^{-3}$) around 34°N , 118°W for both categories of days,
550 which is close to the Ports of Los Angeles and Long Beach, two of the busiest container ports (in terms of cargo
551 volume processed) in the United States and areas with elevated levels of NO_x and SO_x due to the ship exhaust and
552 port emissions (Corbett and Fischbeck, 1997). As can be seen in the Fig. S5, the ABF concentrations around 34°N ,
553 118°W and 38°N , 122°W increase throughout the day, with more significant increases north of the ports for southerly
554 flow days. On southerly flow days, NAAPS results point to marked enhancements in fine aerosol and smoke mass
555 concentration north of Pt. Reyes over water but with mostly a reduction in such values to the south of Pt. Reyes over
556 water. ABF represents the category of species that are most tied to the tracer species shown already to be enhanced in
557 southerly flow, and thus at least this result from NAAPS is consistent with enhanced values across most of the study
558 domain in southerly flow.

559 3.2.3 Supermicron Aerosol

561 While this study hypothesizes that most of the aerosol changes in southerly flow will pertain to submicron
562 aerosol, we still discuss supermicron aerosol characteristics to determine if there was any change observed. Beginning
563 with the aircraft observations, $N_{a>1\mu\text{m}}$ levels were generally low and usually zero in terms of flight median values
564 simply due to so many zero values during a RF. Northerly flow conditions yielded median levels exceeding zero for
565 E-PEACE (1.25 cm^{-3}) and BOAS (1.24 cm^{-3}). In contrast, southerly flow led to levels of 2.51 cm^{-3} and 1.00 cm^{-3}
566 during NiCE and CSM, respectively. The enhancement during southerly flow during at least CSM is presumed to be
567 due to pervasive smoke during many of those RFs. Figure S1 shows a scatterplot of total CASF number concentration
568 versus effective diameter to separate out where cloud droplets are relative to probable sea salt particles and then coarse
569 aerosol associated with the wildfires. There is considerable data coverage at $\text{LWC} < 0.02 \text{ g m}^{-3}$, with effective
570 diameters below $5 \mu\text{m}$ and number concentrations exceeding 10 cm^{-3} , with the latter surpassing what would be
571 expected from sea salt (e.g., Gonzalez et al., 2022). It is very likely that dust particles can be entrained into regional
572 smoke plumes as discussed in past work for the region (e.g., Maudlin et al., 2015; Schlosser et al., 2017). This will be
573 discussed in more detail for a case flight demonstrating such high levels during southerly flow in Sect. 3.4.2.

574 Airborne CW results reveal generally no strong trends in either sea salt or dust tracer species between the flow
575 regimes. The sea salt tracer species Na^+ was lower for southerly days during E-PEACE (and statistically different)
576 and MACAWS ($0.42/1.21$ and $1.30/2.70 \mu\text{g m}^{-3}$ for southerly/northerly days) but with an increase during BOAS (1.99
577 versus $1.55 \mu\text{g m}^{-3}$). The dust tracer species Ca^{2+} was, expectedly, much less abundant compared to Na^+ , without
578 significant differences between flow regimes. However, as already noted (Sect. 3.2.2.2), the fine pollution in southerly
579 flow likely still influenced supermicron aerosol characteristics via Cl^- depletion in salt particles.

580 In terms of IMPROVE data, $\text{PM}_{\text{coarse}}$, Si, fine soil, and Cl^- are the variables that would best coincide with
581 typical sources of supermicron aerosol (i.e., dust and sea salt). They did not reveal any consistent trend for the two
582 campaigns. Based on the lack of a general trend and limited southerly statistics, it is concluded that there is insufficient
583 evidence from IMPROVE to conclude that there is more or less dust or salt influence on southerly days.

584 The wind profile discussed in Sect. 3.1 has implications for sea salt aerosol production, which is influenced by
585 wind speed. The breaking of wave crests to produce (mostly coarse mode) spray droplets occurs at strong wind
586 conditions ($>10 \text{ m s}^{-1}$) (Monahan et al., 1986). Additionally, jet droplets are produced via bubble bursting at lower
587 wind speeds ($>5 \text{ m s}^{-1}$; Blanchard and Woodcock, 1957; Fitzgerald, 1991; Wu, 1992; Moorthy and Sathesh, 2000).
588 On southerly days, there were faster northerly winds over the open ocean offshore west of 125°W , which
589 corresponded to high sea salt concentrations ($>100 \mu\text{g m}^{-3}$) according to NAAPS, whereas northerly days had slower



590 v_{wind} and less sea salt ($65 - 90 \mu\text{g m}^{-3}$) in those same areas farther offshore. In contrast, in the coastal areas south of
591 35°N , northerly days had higher sea salt concentrations (by $10 - 20 \mu\text{g m}^{-3}$) than southerly days with weaker (less
592 negative) v_{wind} . NAAPS shows the same general trends for coarse aerosol mass compared to sea salt, with dust being
593 far less abundant and more spatially heterogeneous in terms of enhancements and reductions between southerly and
594 northerly conditions. In general, the NAAPS results are consistent with aircraft and IMPROVE results in that in the
595 study domain, there was not any pronounced difference in coarse aerosol characteristics during southerly flow.

596

597 **3.3 Cloud Responses**

598 **3.3.1 Airborne In Situ Results**

599 As most campaigns exhibited higher N_d on southerly flight days, it matches expectation that most campaigns
600 exhibited higher N_d values for southerly days (southerly/northerly values): E-PEACE ($252/163 \text{ cm}^{-3}$), BOAS ($143/127$
601 cm^{-3}), MACAWS ($189/165 \text{ cm}^{-3}$), and CSM ($334/314 \text{ cm}^{-3}$). These campaigns had southerly N_d values that were \sim
602 $20 \pm 4 \text{ cm}^{-3}$ greater than the median values on northerly days, with a significant difference during E-PEACE ($\Delta N_d \sim$
603 89 cm^{-3}). E-PEACE also had the best cloud data statistics compared to the other missions, qualifying it as the most
604 robust campaign for inspection of cloud properties. The remaining two campaigns had the least amount of cloud data
605 during southerly flow conditions (NiCE and FASE) and thus those results are of less importance to discuss. CSM had
606 the highest N_d concentrations for both southerly and northerly days due to the strongest levels of pollution (from
607 smoke) relative to the other campaigns.

608

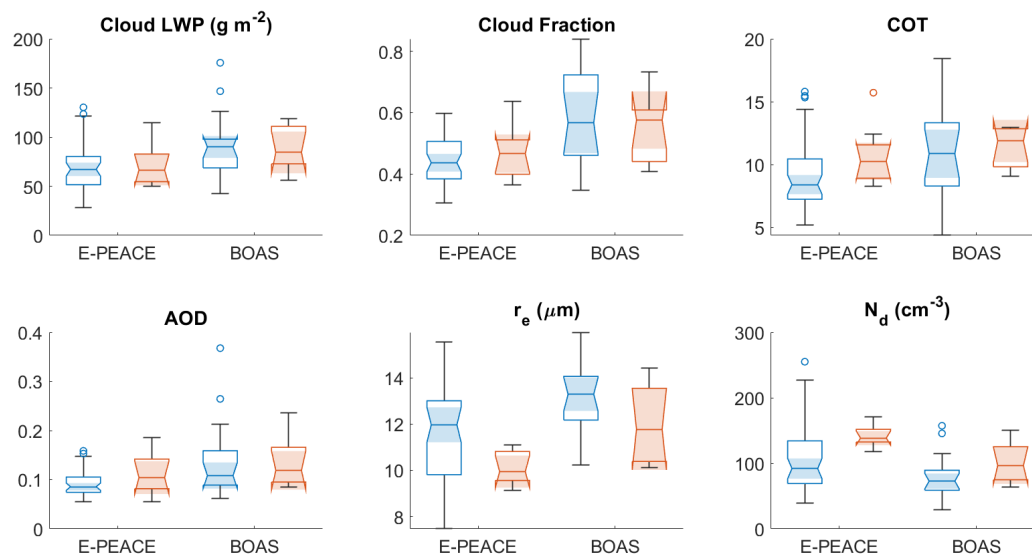
609 **3.3.2 Satellite Data Results**

610 The second part of our hypothesis was that there would be a noticeable difference in cloud properties like N_d , r_e ,
611 and COT between southerly and northerly flow days (at fixed LWP), namely due to the change in emissions sources.
612 In particular, we anticipated higher N_d and COT and lower r_e for southerly flow periods due to the Twomey effect
613 (Twomey, 1974) and higher particle concentrations from continental pollution and shipping emissions. Six parameters
614 were retrieved from MODIS, divided into southerly and northerly days for E-PEACE and BOAS, and visualized as
615 box plots (Fig. 5). Cloud LWP medians for southerly and northerly days within E-PEACE ($66.48/67.17 \text{ g m}^{-2}$) and
616 BOAS ($84.40/89.90 \text{ g m}^{-2}$) were not significantly different. Therefore, these two campaigns are the focus here, unlike
617 the other campaigns that had larger differences (Table S7). The medians for N_d were higher for southerly days
618 ($138.54/91.99 \text{ cm}^{-3}$ and $96.59/72.80 \text{ cm}^{-3}$ for southerly/northerly wind days during E-PEACE and BOAS,
619 respectively), and the southerly and northerly medians during E-PEACE were significantly different from one another.
620 Consistent with the Twomey effect (Twomey, 1974), the median r_e for southerly flow days was lower than northerly
621 flow days ($9.94/11.97 \mu\text{m}$ and $11.77/13.29 \mu\text{m}$), with the medians during E-PEACE being significantly different.
622 Cloud optical thickness was also higher for southerly days compared to northerly days for both campaigns ($10.27/8.42$
623 and $11.88/10.87$ for E-PEACE and BOAS, respectively); however, the medians for each flow regime were not found
624 to be significantly different from one another. We note that even NiCE with LWP values being slightly higher for
625 southerly days (82.78 g m^{-2} versus 74.54 g m^{-2}), the same general results are observed with southerly days having
626 higher N_d /COT and reduced r_e (Table S7); the other three campaigns did not follow these N_d /COT/ r_e trends due to the
627 larger LWP differences between flow regimes.

628

629 Although no differences were necessarily expected, we still examined cloud fraction and AOD, which were
630 similar within a campaign for the two types of days ($0.47/0.44$ versus $0.58/0.57$, and $0.10/0.09$ versus $0.12/0.11$,
631 respectively, for southerly and northerly wind days during E-PEACE versus BOAS). Based on these results, N_d , r_e ,
632 and COT differences between flow regimes match our hypothesis, and two out of the three parameters during E-
633 PEACE were found to be significantly different between southerly and northerly days.

634



634 **Figure 5:** Box plots of MODIS data within the study region during the periods overlapping with E-PEACE and BOAS. The
635 southerly data for E-PEACE and BOAS (eight points each) are represented by the red boxes, and the northerly data (44
636 and 17 points, respectively) are represented by the blue boxes. The notches (and shading, which helps to more clearly
637 indicate where the notches end) of the boxes assist in the determination of significance between multiple medians. If the
638 notches overlap, the medians are not significantly different from one another.
639
640

641 3.4 Case Studies

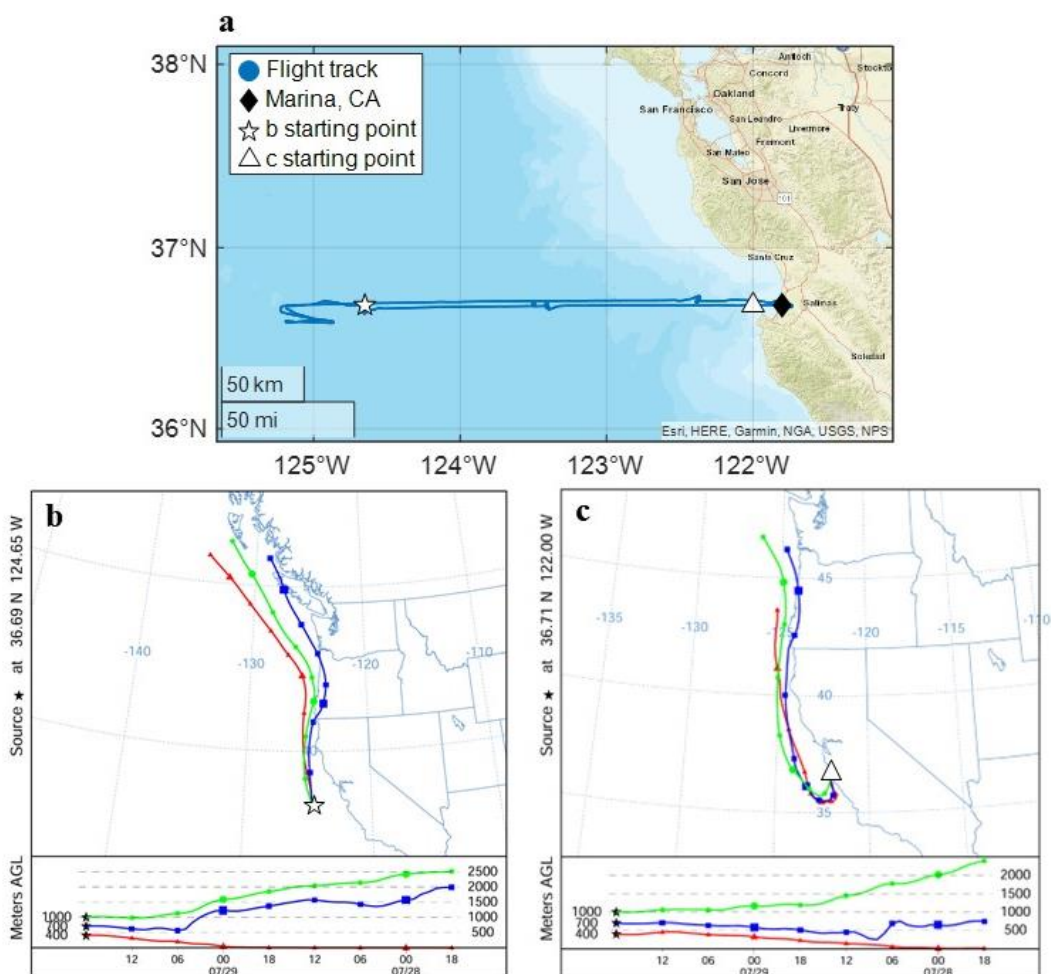
642 In addition to looking at whole campaigns, we also looked closely at two RFs with southerly wind direction:
643 NiCE RF 16 (29 July 2013) and CSM RF 6 (10 September 2020). NiCE RF 16 was a unique flight, which coincided
644 with a CTD event (Bond et al., 1996; Nuss, 2007) and its flight path extended past 125° W into a large stratocumulus
645 cloud clearing (Crosbie et al., 2016; Dadashazar et al., 2020), which was unusual for the Twin Otter flights. CSM RF
646 6 was on a heavily polluted day owing to biomass burning emissions during one of the worst wildfire periods in CA
647 history.
648

649 3.4.1 NiCE Research Flight 16

650 NiCE RF 16 (29 July 2013) occurred on a day with a large stratocumulus cloud deck clearing, which, at its
651 widest point, was 150 km (Crosbie et al., 2016). As noted in Crosbie et al. (2016), this was a CTD event during the
652 time of the flight, and the boundary layer wind reversal (and resulting northwesterly flow) occurred under the
653 stratocumulus cloud deck within 100 km of the coast (~ 36.7° N, 123° W). The location of the wind reversal was
654 known, which allowed us to investigate if there was any apparent gradient in aerosol and cloud variables from the
655 coast to out over the ocean. The aircraft departed from Marina at approximately 1700 UTC, with a nearly straight,
656 westward path (Fig. 6a) toward the clear-cloudy boundary (reader is referred to Fig. 1a of Crosbie et al., 2016 for
657 boundary location). At the clear-cloudy interface (~ 36.7° N, 125° W, 1845 – 2000 UTC), stacked legs were performed
658 at multiple levels in both the MBL and FT on both sides of the boundary. Subsequently, the aircraft returned to Marina
659 following the initial outbound path. To visualize the location and general timing of the wind reversal (Fig. 6b-c), 48-
660 hr back-trajectories from HYSPLIT were used. This contrasts with the 24-hr back trajectories used to confirm
661 southerly wind flow in Sect. 2.2. For the case studies, 48-hr periods were used to have a better understanding of air
662 mass history. This case of southerly wind is one where the sampled air mass was likely to have spent more time in the
663 coastal area just south of Marina as compared to traditional northerly flow, where there was presumed influence from
664 shipping emissions and possibly advected continental air.



665



666

667

668

669

670

671

672

673

674

675

676

677

678

679

680

681

Figure 6: (a) NiCE RF 16 (07/29/2013) flight track, with Marina represented by a solid black diamond, the starting point of the HYSPLIT back-trajectory in panel (b) indicated by a white star, and the starting point of the HYSPLIT back-trajectory in panel (c) indicated by a white triangle. (b) 48-hour back trajectory of a point (36.69° N, 124.65° W) along the flight path outside of the southerly wind zone (HYSPLIT end time: 1800 UTC). (c) 48-hour back trajectory of a point (36.71° N, 122.00° W) along the flight path at the beginning of the RF (HYSPLIT end time: 1700 UTC) where there was southerly flow. Panels (b) and (c) detail back-trajectories for three different altitudes: 400, 700, and 1000 m.

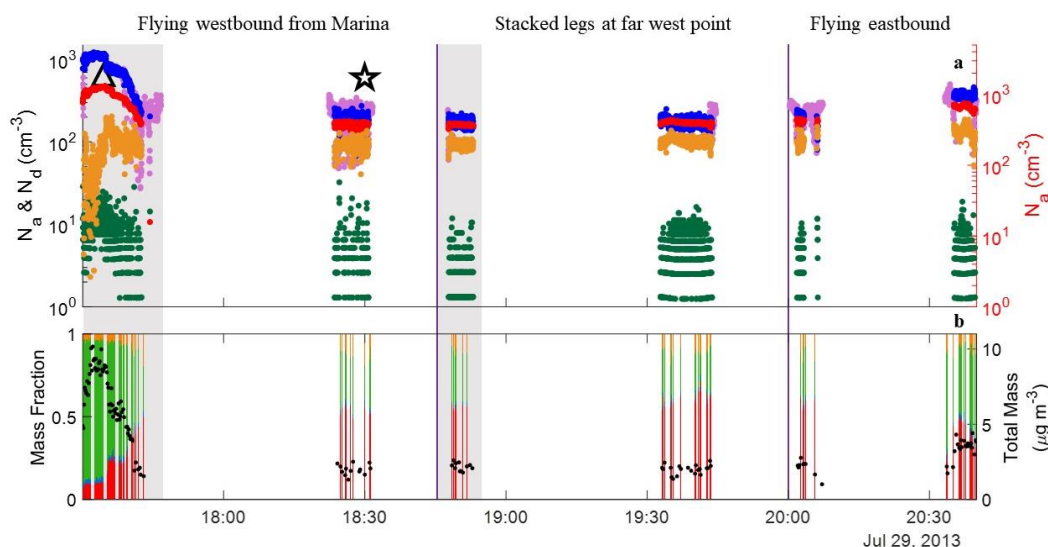
We investigated gradients from the coast to farther offshore including past the wind reversal for several parameters, including N_a , N_d , and AMS total mass and mass fractions, both in the sub-cloud MBL (<525 m AGL, Fig. 7) and in the FT (>765 m AGL, Fig. S12), both altitudes of which were defined in Crosbie et al. (2016). There was a general trend of decreasing number concentration, especially for $N_{a0.1-1\mu m}$, $N_{a>10nm}$, and N_d , from the coast to slightly before the stacked legs at the far west point (1,245/189, 1,240/390, and 772/263 cm^{-3} , respectively, at ~1732/1830 UTC). There was a wide range of supermicron concentrations for the whole flight duration, however, generally, there was a slight decrease of $N_{a>1\mu m}$ along the flight path going west as well, but it was not as pronounced as the other variables (24/4 cm^{-3}).



682 The eastbound leg to Marina was an interesting situation as there was no longer southerly flow closer to the
 683 coast yet there was still a concentration increase for number and cloud drop concentrations but not up to the same
 684 maximum levels that were observed on the westbound portion of the flight, probably owing to the reduced influence
 685 from areas south of the sampling area ($N_{a0.1-1\mu\text{m}}$: 248/435, $N_{a>10\text{nm}}$: 454/752, N_d : 272/434, and $N_{a>1\mu\text{m}}$: 5/19 cm^{-3} , for
 686 eastbound/westbound legs at ~2000/2037 UTC). AMS mass concentrations dropped significantly in the outbound
 687 portion of the flight, from total mass as high as 10.16 $\mu\text{g m}^{-3}$ (~1730 UTC) to 1.55 $\mu\text{g m}^{-3}$ (~1745 UTC), the latter of
 688 which was approximately 10 km offshore. During that period, organic mass fraction decreased from 0.81 to 0.28 in
 689 favor of growing SO_4^{2-} mass fraction from 0.11 to 0.50. On the inbound track, similar to N_a/N_d results, there was not
 690 as much of an enhancement in total mass (max of 4.41 $\mu\text{g m}^{-3}$ at ~2040 UTC) and the chemical profile revealed more
 691 comparable levels of SO_4^{2-} and organic mass fractions (0.39 and 0.52, respectively, at ~2040 UTC) in contrast to the
 692 outbound track that showed higher organic mass fraction right by the coast.

693 The results suggest that the enhanced residence time of air masses (due to the wind reversal) in an area with
 694 presumed influence from shipping emissions and continental pollution yielded an offshore gradient in N_a , N_d , and
 695 aerosol composition. Also, the results help show that this general coastal zone area in the location of the wind reversal
 696 is enhanced with fine pollution, which generally will affect aerosol and cloud characteristics if air masses spend
 697 prolonged time in it during southerly flow conditions.

698



699 **Figure 7: Data from NiCE RF 16 in the MBL (<525 m). The grey shading indicates time periods with mostly southerly**
 700 **winds, and the purple lines across all graphs indicate flight zones (outbound track, stacked legs at farthest west point, and**
 701 **inbound track). (a) The colored points on the left-hand axis correspond to $N_{a0.1-1\mu\text{m}}$ (blue, PCASP $_{<1\mu\text{m}}$), $N_{a>1\mu\text{m}}$ (green,**
 702 **PCASP $_{>1\mu\text{m}}$), and N_d (light purple, CASF). The colored points on the right-hand axis correspond to $N_{a>10\text{nm}}$ (red, CPC) and**
 703 **$N_{a10-100\text{nm}}$ (yellow, CPC 3010 – PCASP $_{<1\mu\text{m}}$). The triangle corresponds to the HYSPLIT back-trajectory end point seen in**
 704 **Fig. 6c, and the star corresponds to the HYSPLIT back-trajectory end point seen in Fig. 6b. (b) Stacked bar plot of AMS**
 705 **mass fractions of SO_4^{2-} (red), NO_3^- (blue), organics (green), and NH_4^+ (orange), overlaid with total mass concentration (μg**
 706 **m^{-3} ; black).**
 707
 708

709 The trends in the FT are much more ambiguous than those in the MBL (Fig. S12). Similar to the MBL, there
 710 was a decrease in $N_{a0.1-1\mu\text{m}}$ and $N_{a>10\text{nm}}$ from the coast to near the stacked legs (2,467/395 and 2,820/689 cm^{-3} ,
 711 respectively, at ~1726/1844 UTC), however there was no discernable trend for $N_{a>1\mu\text{m}}$. There were no apparent
 712 offshore trends for AMS total mass or speciated mass fractions. Additionally, on the eastbound flight leg, there was
 713 not a clear trend for any of the parameters. This suggests that the effects of the southerly winds were stronger in the
 714 MBL than the FT.

715

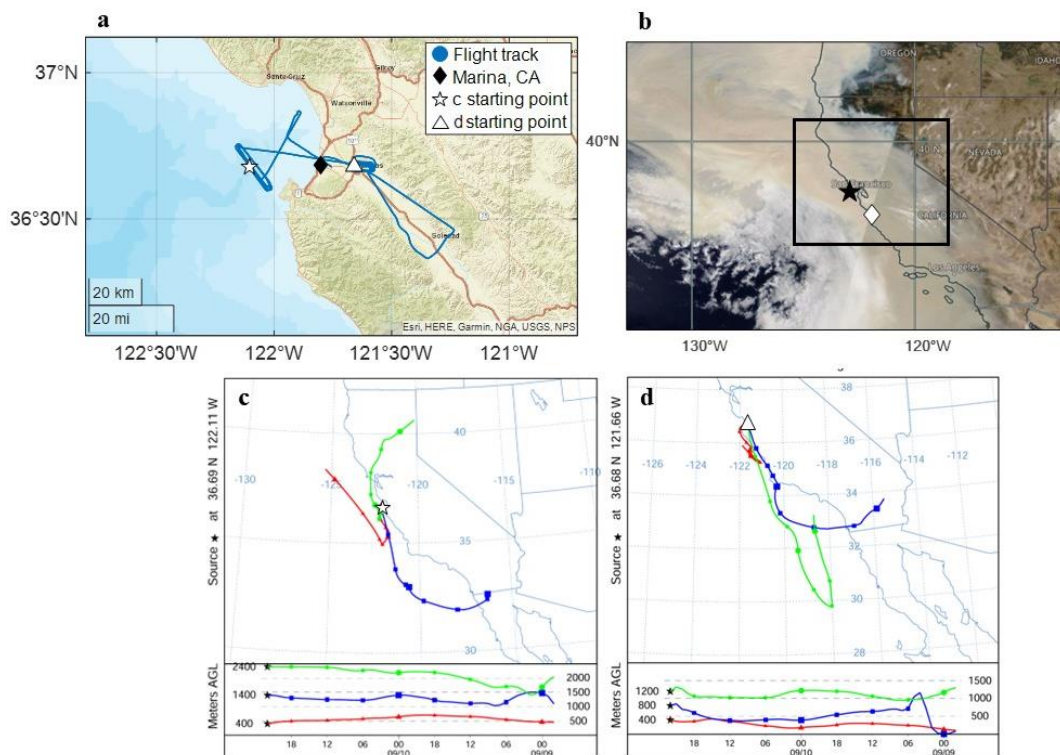


716 3.4.2 CSM Research Flight 6

717 CSM stands out among all of the examined campaigns owing to the strength and temporal persistence of
718 wildfire plumes, which was also the main focus of the mission. Of the top 3% ($n = 12$) of the largest fires in the
719 historical record, four occurred in 2020 (circled in Fig. 3): the August Complex fire (16 August, Mendocino County),
720 the SCU Lightning Fire Complex (18 August, Santa Clara County), the Creek fire (4 September, Madera County),
721 and the LNU Lightning Complex fire (16 August, Hapa County) (Keeley and Syphard, 2021). These four fires were
722 a mix of both merged (August Complex) and unmerged (LNU Lightning Complex) fires that burned over 417, 160,
723 153, and 146 kha, respectively, and burned for months after they were ignited.

724 CSM RF 6 (10 September 2020) included two major components (Fig. 8a): a spiral over Salinas (max altitude
725 of 6,172 m at ~2000 UTC) and a spiral over Monterey Bay (max altitude of 4,822 m at ~2170 UTC). The entire region
726 was heavily impacted by smoke during CSM RF 6 (Fig. 8b). Additionally, around 36.5° N, 125° W, there is an area
727 not dominated by smoke, but rather, clouds, pointing to the likelihood of smoke-cloud interactions in the region on
728 not just this day but other CSM days with similar smoky conditions. HYSPLIT back-trajectories for the two spirals
729 for a 48-hr period were generated (Fig. 8c and 8d). For the spiral over Monterey Bay (Fig. 8c), the lowest altitude
730 trajectory (trajectory beginning at 400 m) is mostly northwesterly, the second lowest altitude (trajectory beginning
731 at 1400 m) is primarily southerly, and the highest altitude (trajectory beginning at 2400 m) is approximately
732 northeasterly. The highest altitude back-trajectory passes over the LNU Lightning Complex fire (red oval; circled in
733 Fig. 3). For the spiral over Salinas (Fig. 8d), all three altitude levels (400, 800, and 1200 m AGL) reveal southerly
734 trajectory paths, and the air masses from the second-highest altitude back-trajectory possibly had some influence from
735 the SCU Lightning Fire Complex (purple oval) and the August Complex Fire (green oval) due to offshore and
736 northerly flow in the preceding 36-hr (Fig. 3).

737



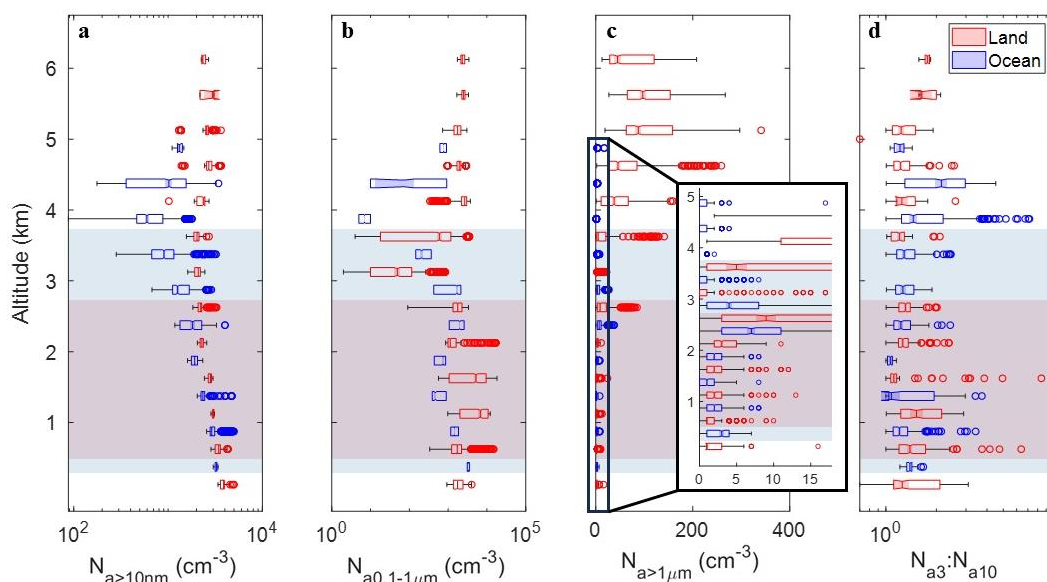
738
739 **Figure 8:** (a) CSM RF 6 (09/10/2020) flight track, with Marina, CA represented by a solid black diamond, the starting point
740 of the HYSPLIT back-trajectory in panel (c) indicated by a white star, and the starting point of the HYSPLIT back-
741 trajectory in panel (d) indicated by a white triangle. (b) NASA Worldview image, with Marina, CA represented by a white



742 diamond, and Pt. Reyes denoted by a black star. (c) 48-hour back trajectory of a point (36.69° N, 122.11° W) along the flight
 743 path during the sounding over Monterey Bay (HYSPLIT end time: 2100 UTC) at three different altitudes: 400, 1400, and
 744 2400 m. (b) 48-hour back trajectory of a point (36.68° N, 121.66° W) along the flight path during the sounding over Salinas
 745 (HYSPLIT end time: 1900 UTC) at three different altitudes: 400, 800, and 1200 m. (c) and (d) utilized different altitudes
 746 for the back-trajectories to reflect the different maximum altitudes of the two major soundings of the flight.
 747

748 The vertical profiles of temperature, wind speed, and wind direction are provided in Fig. S13 for context.
 749 Notably, the vertical region with southerly flow was thicker over the ocean (approximately 370 – 3700 m) versus over
 750 land (540 – 2900 m). N_a for different size ranges and $N_{a3}:N_{a10}$ are shown separately for land and over the ocean (Fig.
 751 9). There was more variability in $N_{a>10nm}$ (Fig. 9a) over the ocean, with a general decrease in concentration with
 752 increase in altitude for both data over land and ocean, followed by increasing $N_{a>10nm}$ above of the region of primarily
 753 southerly flow (non-shaded points). There was not much change in $N_{a>1\mu m}$ (medians = 1 – 3 cm^{-3} ; range = 0 – 6 cm^{-3} ;
 754 Fig. 9c) until >2.5 km, where concentration increases over land (medians = 5 – 97 cm^{-3} ; range = 0 – 297 cm^{-3}) where
 755 there is primarily northerly flow, likely from sampling smoke plumes. Over the ocean, low supermicron particle
 756 concentrations are observed ($\leq 7 \text{ cm}^{-3}$). These results show that during extensive smoky periods, the flow regime does
 757 not matter in cases like RF6 due to smoke generally being all across the region. Furthermore, the results show that
 758 supermicron particle concentrations are certainly enhanced in smoke plumes, as has been observed before in the study
 759 region (Mardi et al., 2018) but not to this pronounced extent, especially at high altitudes over land.

760 The $N_{a3}:N_{a10}$ ratio (Fig. 9d) was generally consistent over land across all vertical levels, with a good number
 761 of outliers in the region of primarily southerly flow. The medians of the ratios over the ocean were usually lower than
 762 the medians over land until 3.5 km. There was no discernable difference in the $N_{a3}:N_{a10}$ ratio over land between
 763 southerly and northerly flow (medians approximately 1.35 until >5.5 km) or over the ocean (medians for both flow
 764 regimes approximately 1.20, with a slight bump to 1.26 and 2.14 between 3.5 and 4.5 km).
 765



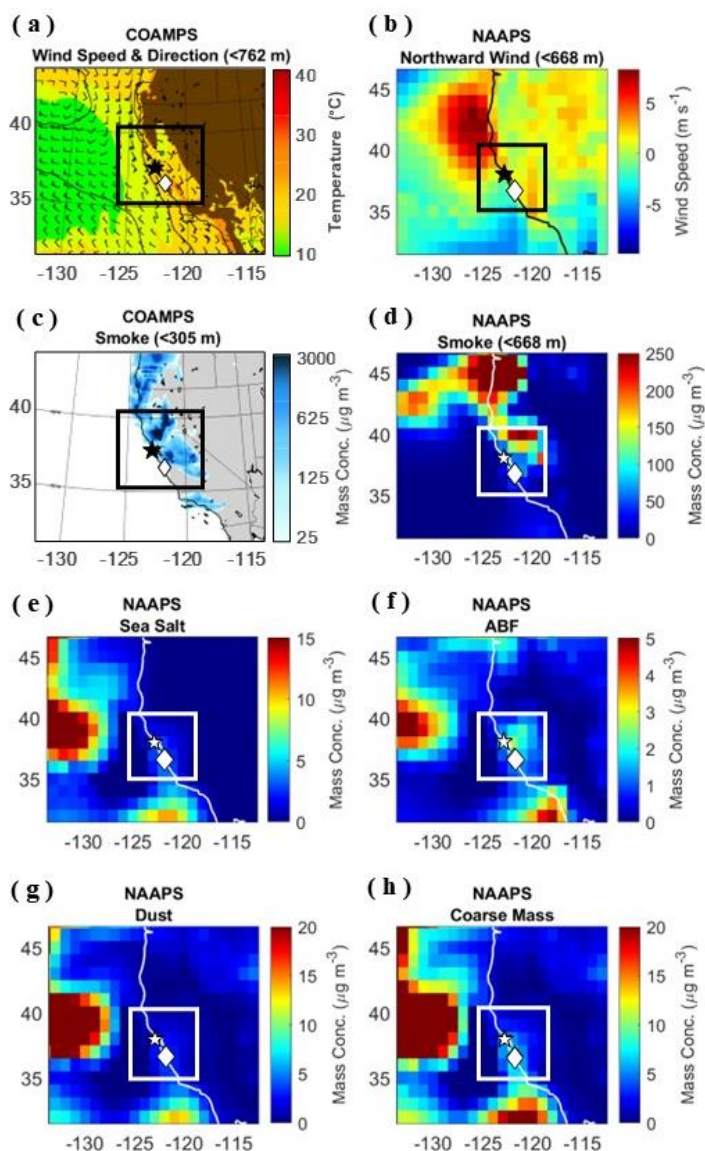
766 **Figure 9:** CSM RF 6 box plot vertical profiles of (a) $N_{a>10nm}$ (cm^{-3}), (b) $N_{a0.1-1\mu m}$ (cm^{-3} ; PCASP $_{<1\mu m}$), (c) $N_{a>1\mu m}$ (cm^{-3} ;
 767 PCASP $_{>1\mu m}$), and (d) $N_{a3}:N_{a10}$. Data are shown every 500 m over land (red) and ocean (blue) above the MBL, which is the
 768 maximum altitude of the first bins for all the panels. Panel (c) has an additional focus on altitudes ≤ 5 km ($N_{a>1\mu m} \leq 18 \text{ cm}^{-3}$).
 769 The red and blue shading indicates altitudes over the land and ocean, respectively, with southerly winds.
 770
 771

772 Complementary data from NAAPS and COAMPS are shown in Fig. 10 for this case flight. COAMPS and
 773 NAAPS (Fig. 10a and 10b, respectively) both show southerly winds generally in the outlined study domain, which is



774 consistent with observational data showing southerly winds close to Marina. NAAPS shows stronger southerly winds
775 over land near Marina compared to over Monterey Bay whereas there was not much of a difference in wind speed
776 between the two spiral soundings from the Twin Otter (Fig. S13). COAMPS better simulates southerly flow along the
777 coastline, whereas the spatial resolution of NAAPS is probably a reason for it not being able to capture southerly flow
778 in the grid spaces closest to the coast especially just south of Marina – instead there is weak northerly flow.

779 A notable difference between NAAPS and COAMPS when it comes to modeling smoke (Fig. 10c and 10d,
780 respectively) is that NAAPS better represents smoke over the ocean and more closely matches the visible satellite
781 imagery from Fig. 8b. COAMPS does not capture smoke over the ocean away from the coastline. We do not focus on
782 comparing absolute mass concentrations of smoke as it is difficult to know the ground truth value from the aircraft
783 observations and also because of the different ways and size classifications for smoke in the two models. Generally,
784 though, NAAPS and COAMPS match in the general areas identified as having smoke and areas of high concentrations
785 match one another. Looking at Fig. 10e, NAAPS shows high concentrations of sea salt offshore west of 130° W.
786 However, near the flight area and within our region of focus, sea salt concentrations are less than 5 $\mu\text{g m}^{-3}$. NAAPS
787 ABF (Fig. 10f) mirrors the areas with areas of high sea salt in Fig. 10e, but similar to model results from Sect. 3.2.2.4,
788 there are areas of higher ABF concentrations (2 – 3 $\mu\text{g m}^{-3}$) near the ports of Los Angeles and Long Beach (34° N,
789 118° W) as well as up north near San Francisco and San Jose (38° N, 122° W). NAAPS dust (Fig. 10g) and coarse
790 mass (Fig. 10h) also resemble the areas with high sea salt, with coarse mass concentrations exceeding 10 $\mu\text{g m}^{-3}$ near
791 both Marina, CA and Pt. Reyes.
792



793
794 **Figure 10:** COAMPS/NAAPS images are for 2100 UTC. (a) Wind speed and direction up to 762 m derived from COAMPS.
795 The colors indicate surface temperature (°C). (b) Wind speed of northward wind up to 668 m derived from NAAPS. (c)
796 Smoke concentration ($\mu\text{g m}^{-3}$) up to 305 m derived from COAMPS. (d) Smoke, (e) sea salt, (f) ABF, (g) dust, and (h)
797 coarse mass concentrations ($\mu\text{g m}^{-3}$) up to 668 m derived from NAAPS. The white diamond indicates Marina, CA, the white star
798 indicates Pt. Reyes, and the black & white boxes indicate our zone of interest.
799

800 4 Conclusions

801 In this study, we utilized multiple types of data, including a large repository of NPS Twin Otter data, to
802 compare coastal aerosol and cloud characteristics near central CA for northerly and southerly wind regimes in the
803 lower troposphere. Juliano et al. (2019a) had previously called for future studies to utilize in situ observations to
804 support their investigation into cloud properties using satellite observations. Our study is the first to investigate aerosol



805 and cloud droplet number concentrations through in situ aircraft data in addition to CW composition, and intercompare
806 those results with satellite data, as well as models and surface station data.

807 Our first hypothesis is proven correct in that more fine aerosol pollution is present off the CA coast during
808 southerly flow due to influence from shipping exhaust and continental emissions including from major cities like Los
809 Angeles. Submicron aerosol pollution is found to be higher during southerly flow days (particularly during E-PEACE),
810 with respect to both N_a ($N_{a>10nm}$, $N_{a10-100nm}$, $N_{a0.1-1\mu m}$) and concentrations of shipping and continental tracer species in
811 surface data (SO_4^{2-} , NO_3^- , OC, V, Ni, and EC) and CW samples (nss- SO_4^{2-} , NO_3^- , NH_4^+ , V and oxalate). Cloud water
812 is shown to be more acidic during southerly flow along with more Cl^- depletion based on lower $Cl^-:Na^+$ ratios. A
813 secondary hypothesis was that increased influence from shipping and/or continental emissions would lead to enhanced
814 N_d and COT and lower r_e (at fixed LWP) due to the Twomey effect (Twomey, 1974). Both the airborne in situ data
815 and satellite retrievals show increased N_d on southerly days. The satellite retrieval data also reveal higher COT and
816 lower r_e during southerly flow. The increase in N_d and decrease in r_e associated with the northerly to southerly reversal
817 matches results of a previous study in the region (Juliano et al., 2019a). The analysis of CSM RF 6 reveals that during
818 heavy biomass burning periods with prevailing smoke, there is relatively no difference in aerosol or cloud properties
819 associated with changes in flow regime.

820 A limitation in this type of study to address in the future is the difficulty of obtaining detailed in situ data
821 during southerly wind conditions. As noted already, wind reversals along coasts extend to a number of other global
822 regions (e.g., South America, southern Africa, Australia) and thus it is recommended to continue building more
823 statistics to better understand changes in aerosol and cloud properties as a function of wind direction along coastal
824 regions. Intercomparisons with models, as partly done here, can aid with determining if model resolution should
825 improve to better simulate these events. Generally speaking, the prevalence of fine aerosol on southerly flow days and
826 associated changes in cloud microphysical properties are important findings with implications for weather, health,
827 coastal ecology, and aviation.

828

829 **Data availability**

830 Airborne data used in this work can be accessed at <https://doi.org/10.6084/m9.figshare.5099983.v11> (Sorooshian et
831 al., 2017). Bouy data from the NOAA's NDBC can be accessed at <https://www.ndbc.noaa.gov/>. The archived data
832 from GOES-West Full Disk Cloud Product (GOES-15) can be accessed at <https://satcorps.larc.nasa.gov/>. The archived
833 surface weather plots from NOAA's WPC can be accessed at
834 https://www.wpc.ncep.noaa.gov/archives/web_pages/sfc/sfc_archive.php. The surface data from IMPROVE can be
835 accessed at <http://views.cira.colostate.edu/fed/>. The MODIS-Aqua data can be accessed through NASA Giovanni at
836 <https://giovanni.gsfc.nasa.gov/giovanni/>. The FIRMS data can be accessed at <https://earthdata.nasa.gov/firms>.

837 **Author contributions**

838 AW and PX aided with access and interpretation of COAMPS and NAAPS data, respectively. KZ and GB conducted
839 the data analysis. KZ and AS conducted data interpretation. KZ and AS prepared the manuscript. All authors edited
840 the manuscript.

841 **Competing interests**

842 At least one of the (co-)authors is a member of the editorial board of Atmospheric Chemistry and Physics.

843 **Disclaimer**

844 Publisher's note: Copernicus Publications remains neutral with regard to jurisdictional claims in published maps and
845 institutional affiliations.



846

847 **Acknowledgements**

848 The authors acknowledge NPS staff for successfully conducting Twin Otter flights and all others who were involved
849 in the airborne campaigns. We thank Ewan Crosbie for useful discussions about this work.

850 **Financial support**

851 This work was funded by Office of Naval Research grant N00014-21-1-2115.

852

853

854 **References**

855

856 AzadiAghdam, M., Braun, R. A., Edwards, E.-L., Bañaga, P. A., Cruz, M. T., Betito, G., Cambaliza, M. O.,
857 Dadashazar, H., Lorenzo, G. R., Ma, L., MacDonald, A. B., Nguyen, P., Simpas, J. B., Stahl, C., and Sorooshian, A.:
858 On the nature of sea salt aerosol at a coastal megacity: Insights from Manila, Philippines in Southeast Asia,
859 *Atmospheric Environment*, 216, 116922, <https://doi.org/10.1016/j.atmosenv.2019.116922>, 2019.

860 Blanchard, D. C. and Woodcock, A. H.: Bubble Formation and Modification in the Sea and its Meteorological
861 Significance, *Tellus*, 9, 145-158, 10.3402/tellusa.v9i2.9094, 1957.

862 Bond, N. A., Mass, C. F., and Overland, J. E.: Coastally Trapped Wind Reversals along the United States West
863 Coast during the Warm Season. Part I: Climatology and Temporal Evolution, *Monthly Weather Review*, 124, 430-
864 445, [https://doi.org/10.1175/1520-0493\(1996\)124<0430:CTWRAT>2.0.CO;2](https://doi.org/10.1175/1520-0493(1996)124<0430:CTWRAT>2.0.CO;2), 1996.

865 Braun, R. A., Dadashazar, H., MacDonald, A. B., Aldhaif, A. M., Maudlin, L. C., Crosbie, E., Aghdam, M. A.,
866 Hossein Mardi, A., and Sorooshian, A.: Impact of Wildfire Emissions on Chloride and Bromide Depletion in Marine
867 Aerosol Particles, *Environmental Science & Technology*, 51, 9013-9021, 10.1021/acs.est.7b02039, 2017.

868 Cahill, T. A., Ashbaugh, L. L., Eldred, R. A., Feeney, P. J., Kusko, B. H., and Flocchini, R. G.: Comparisons
869 Between Size-Segregated Resuspended Soil Samples and Ambient Aerosols in the Western United States, in:
870 *Atmospheric Aerosol*, ACS Symposium Series, 167, AMERICAN CHEMICAL SOCIETY, 269-285,
871 doi:10.1021/bk-1981-0167.ch015

872 10.1021/bk-1981-0167.ch015, 1981.

873 Celso, V., Dabek-Zlotorzynska, E., and McCurdy, M.: Chemical Characterization of Exhaust Emissions from
874 Selected Canadian Marine Vessels: The Case of Trace Metals and Lanthanoids, *Environmental Science &*
875 *Technology*, 49, 5220-5226, 10.1021/acs.est.5b00127, 2015.

876 Chow, J. C., Watson, J. G., Pritchett, L. C., Pierson, W. R., Frazier, C. A., and Purcell, R. G.: The dri thermal/optical
877 reflectance carbon analysis system: description, evaluation and applications in U.S. Air quality studies, *Atmospheric*
878 *Environment. Part A. General Topics*, 27, 1185-1201, [https://doi.org/10.1016/0960-1686\(93\)90245-T](https://doi.org/10.1016/0960-1686(93)90245-T), 1993.

879 Coggon, M. M., Sorooshian, A., Wang, Z., Craven, J. S., Metcalf, A. R., Lin, J. J., Nenes, A., Jonsson, H. H.,
880 Flagan, R. C., and Seinfeld, J. H.: Observations of continental biogenic impacts on marine aerosol and clouds off the
881 coast of California, *Journal of Geophysical Research: Atmospheres*, 119, 6724-6748, 10.1002/2013jd021228, 2014.

882 Coggon, M. M., Sorooshian, A., Wang, Z., Metcalf, A. R., Frossard, A. A., Lin, J. J., Craven, J. S., Nenes, A.,
883 Jonsson, H. H., Russell, L. M., Flagan, R. C., and Seinfeld, J. H.: Ship impacts on the marine atmosphere: insights
884 into the contribution of shipping emissions to the properties of marine aerosol and clouds, *Atmospheric Chemistry*
885 *and Physics*, 12, 8439-8458, 10.5194/acp-12-8439-2012, 2012.

886 Corbett, J. J. and Fischbeck, P.: Emissions from Ships, *Science*, 278, 823-824, doi:10.1126/science.278.5339.823,
887 1997.

888 Corbin, J. C., Mensah, A. A., Pieber, S. M., Orasche, J., Michalke, B., Zanatta, M., Czech, H., Massabò, D., Buatier
889 de Mongeot, F., Mennucci, C., El Haddad, I., Kumar, N. K., Stengel, B., Huang, Y., Zimmermann, R., Prévôt, A. S.
890 H., and Gysel, M.: Trace Metals in Soot and PM_{2.5} from Heavy-Fuel-Oil Combustion in a Marine Engine,
891 *Environmental Science & Technology*, 52, 6714-6722, 10.1021/acs.est.8b01764, 2018.

892 Council, N. R.: *Coastal Meteorology: A Review of the State of the Science*, Washington, D.C., 99,
893 <https://doi.org/10.17226/1991>, 1992.

894 Crosbie, E., Wang, Z., Sorooshian, A., Chuang, P. Y., Craven, J. S., Coggon, M. M., Brunke, M., Zeng, X., Jonsson,
895 H., Woods, R. K., Flagan, R. C., and Seinfeld, J. H.: Stratocumulus Cloud Clearings and Notable Thermodynamic



896 and Aerosol Contrasts across the Clear–Cloudy Interface, *Journal of the Atmospheric Sciences*, 73, 1083-1099,
897 <https://doi.org/10.1175/JAS-D-15-0137.1>, 2016.

898 Dadashazar, H., Ma, L., and Sorooshian, A.: Sources of pollution and interrelationships between aerosol and
899 precipitation chemistry at a central California site, *Science of The Total Environment*, 651, 1776-1787,
900 <https://doi.org/10.1016/j.scitotenv.2018.10.086>, 2019.

901 Dadashazar, H., Crosbie, E., Majdi, M. S., Panahi, M., Moghaddam, M. A., Behrangi, A., Brunke, M., Zeng, X.,
902 Jonsson, H. H., and Sorooshian, A.: Stratocumulus cloud clearings: statistics from satellites, reanalysis models, and
903 airborne measurements, *Atmospheric Chemistry and Physics*, 20, 4637-4665, 10.5194/acp-20-4637-2020, 2020.

904 Dorman, C. E.: Evidence of Kelvin Waves in California's Marine Layer and Related Eddy Generation, *Monthly*
905 *Weather Review*, 113, 827-839, [https://doi.org/10.1175/1520-0493\(1985\)113<0827:EOKWIC>2.0.CO;2](https://doi.org/10.1175/1520-0493(1985)113<0827:EOKWIC>2.0.CO;2), 1985.

906 Edwards, E. L., Choi, Y., Crosbie, E. C., DiGangi, J. P., Diskin, G. S., Robinson, C. E., Shook, M. A., Winstead, E.
907 L., Ziemba, L. D., and Sorooshian, A.: Sea salt reactivity over the northwest Atlantic: An in-depth look using the
908 airborne ACTIVATE dataset, *EGUsphere*, 2023, 1-56, 10.5194/egusphere-2023-2575, 2023.

909 Ervens, B.: Modeling the Processing of Aerosol and Trace Gases in Clouds and Fogs, *Chemical Reviews*, 115,
910 4157-4198, 10.1021/cr5005887, 2015.

911 Ervens, B., Turpin, B. J., and Weber, R. J.: Secondary organic aerosol formation in cloud droplets and aqueous
912 particles (aqSOA): a review of laboratory, field and model studies, *Atmos. Chem. Phys.*, 11, 11069-11102,
913 10.5194/acp-11-11069-2011, 2011.

914 Fitzgerald, J. W.: Marine aerosols: A review, *Atmospheric Environment. Part A. General Topics*, 25, 533-545,
915 [https://doi.org/10.1016/0960-1686\(91\)90050-H](https://doi.org/10.1016/0960-1686(91)90050-H), 1991.

916 Garreaud, R. and Rutllant, J.: Coastal Lows along the Subtropical West Coast of South America: Numerical
917 Simulation of a Typical Case, *Monthly Weather Review*, 131, 891-908, [https://doi.org/10.1175/1520-0493\(2003\)131<0891:CLATSW>2.0.CO;2](https://doi.org/10.1175/1520-0493(2003)131<0891:CLATSW>2.0.CO;2), 2003.

918 Garreaud, R., Rutllant, J., and Fuenzalida, H.: Coastal Lows along the Subtropical West Coast of South America:
919 Mean Structure and Evolution, *Monthly Weather Review*, 130, 75-88, [https://doi.org/10.1175/1520-0493\(2002\)130<0075:CLATSW>2.0.CO;2](https://doi.org/10.1175/1520-0493(2002)130<0075:CLATSW>2.0.CO;2), 2002.

920 Giglio, L., Schroeder, W., Hall, J. V., and Justice, C. O.: Modis collection 6 active fire product user's guide revision
921 A, Department of Geographical Sciences. University of Maryland, 9, 2015.

922 Gill, A. E.: Coastally trapped waves in the atmosphere, *Quarterly Journal of the Royal Meteorological Society*, 103,
923 431-440, <https://doi.org/10.1002/qj.49710343704>, 1977.

924 Gonzalez, M. E., Corral, A. F., Crosbie, E., Dadashazar, H., Diskin, G. S., Edwards, E.-L., Kirschler, S., Moore, R.
925 H., Robinson, C. E., Schlosser, J. S., Shook, M., Stahl, C., Thornhill, K. L., Voigt, C., Winstead, E., Ziemba, L. D.,
926 and Sorooshian, A.: Relationships between supermicrometer particle concentrations and cloud water sea salt and
927 dust concentrations: analysis of MONARC and ACTIVATE data, *Environmental Science: Atmospheres*, 2, 738-752,
928 10.1039/d2ea00049k, 2022.

929 Guan, S., Jackson, P. L., and Reason, C. J. C.: Numerical Modeling of a Coastal Trapped Disturbance. Part I:
930 Comparison with Observations, *Monthly Weather Review*, 126, 972-990, [https://doi.org/10.1175/1520-0493\(1998\)126<0972:NMOACT>2.0.CO;2](https://doi.org/10.1175/1520-0493(1998)126<0972:NMOACT>2.0.CO;2), 1998.

931 Hegg, D. A., Covert, D. S., and Jonsson, H. H.: Measurements of size-resolved hygroscopicity in the California
932 coastal zone, *Atmos. Chem. Phys.*, 8, 7193-7203, 10.5194/acp-8-7193-2008, 2008.

933 Hilario, M. R. A., Crosbie, E., Baniaga, P. A., Betito, G., Braun, R. A., Cambaliza, M. O., Corral, A. F., Cruz, M. T.,
934 Dibb, J. E., Lorenzo, G. R., Macdonald, A. B., Robinson, C. E., Shook, M. A., Simpas, J. B., Stahl, C., Winstead, E.,
935 Ziemba, L. D., and Sorooshian, A.: Particulate Oxalate-To-Sulfate Ratio as an Aqueous Processing Marker:
936 Similarity Across Field Campaigns and Limitations, *Geophysical Research Letters*, 48, 10.1029/2021gl096520,
937 2021.

938 Hodur, R. M.: The Naval Research Laboratory's Coupled Ocean/Atmosphere Mesoscale Prediction System
939 (COAMPS), *Monthly Weather Review*, 125, 1414-1430, [https://doi.org/10.1175/1520-0493\(1997\)125<1414:TNRLSC>2.0.CO;2](https://doi.org/10.1175/1520-0493(1997)125<1414:TNRLSC>2.0.CO;2), 1997.

940 Hogan, T., Liu, M., Ridout, J., Peng, M., Whitcomb, T., Ruston, B., Reynolds, C., Eckeremann, S., Moskaitis, J.,
941 Baker, N., McCormack, J., Viner, K., McLay, J., Flatau, M., Xu, L., Chen, C., and Chang, S.: The Navy Global
942 Environmental Model, *Oceanography*, 27, 116-125, 10.5670/oceanog.2014.73, 2014.

943 Holland, G. J. and Leslie, L. M.: Ducted coastal ridging over S.E. Australia, *Quarterly Journal of the Royal*
944 *Meteorological Society*, 112, 731-748, <https://doi.org/10.1002/qj.49711247310>, 1986.

945 Juliano, T. W., Lebo, Z. J., Thompson, G., and Rahn, D. A.: A New Perspective on Coastally Trapped Disturbances
946 Using Data from the Satellite Era, *Bulletin of the American Meteorological Society*, 100, 631-651, 10.1175/bams-d-
947 18-0002.1, 2019a.



- 952 Juliano, T. W., Coggon, M. M., Thompson, G., Rahn, D. A., Seinfeld, J. H., Sorooshian, A., and Lebo, Z. J.: Marine
953 Boundary Layer Clouds Associated with Coastally Trapped Disturbances: Observations and Model Simulations,
954 *Journal of the Atmospheric Sciences*, 76, 2963-2993, 10.1175/jas-d-18-0317.1, 2019b.
- 955 Keeley, J. E. and Syphard, A. D.: Large California wildfires: 2020 fires in historical context, *Fire Ecology*, 17,
956 10.1186/s42408-021-00110-7, 2021.
- 957 Lynch, P., Reid, J. S., Westphal, D. L., Zhang, J., Hogan, T. F., Hyer, E. J., Curtis, C. A., Hegg, D. A., Shi, Y.,
958 Campbell, J. R., Rubin, J. I., Sessions, W. R., Turk, F. J., and Walker, A. L.: An 11-year global gridded aerosol
959 optical thickness reanalysis (v1.0) for atmospheric and climate sciences, *Geoscientific Model Development*, 9, 1489-
960 1522, 10.5194/gmd-9-1489-2016, 2016.
- 961 Ma, L., Dadashazar, H., Braun, R. A., MacDonald, A. B., Aghdam, M. A., Maudlin, L. C., and Sorooshian, A.: Size-
962 resolved characteristics of water-soluble particulate elements in a coastal area: Source identification, influence of
963 wildfires, and diurnal variability, *Atmospheric Environment*, 206, 72-84,
964 <https://doi.org/10.1016/j.atmosenv.2019.02.045>, 2019.
- 965 Macdonald, A. B., Dadashazar, H., Chuang, P. Y., Crosbie, E., Wang, H., Wang, Z., Jonsson, H. H., Flagan, R. C.,
966 Seinfeld, J. H., and Sorooshian, A.: Characteristic Vertical Profiles of Cloud Water Composition in Marine
967 Stratocumulus Clouds and Relationships With Precipitation, *Journal of Geophysical Research: Atmospheres*, 123,
968 3704-3723, 10.1002/2017jd027900, 2018.
- 969 Malm, W. C., Sisler, J. F., Huffman, D., Eldred, R. A., and Cahill, T. A.: Spatial and seasonal trends in particle
970 concentration and optical extinction in the United States, *Journal of Geophysical Research: Atmospheres*, 99, 1347-
971 1370, <https://doi.org/10.1029/93JD02916>, 1994.
- 972 Mardi, A. H., Dadashazar, H., Painemal, D., Shingler, T., Seaman, S. T., Fenn, M. A., Hostetler, C. A., and
973 Sorooshian, A.: Biomass Burning Over the United States East Coast and Western North Atlantic Ocean:
974 Implications for Clouds and Air Quality, *Journal of Geophysical Research: Atmospheres*, 126,
975 10.1029/2021jd034916, 2021.
- 976 Mardi, A. H., Dadashazar, H., Macdonald, A. B., Braun, R. A., Crosbie, E., Xian, P., Thorsen, T. J., Coggon, M. M.,
977 Fenn, M. A., Ferrare, R. A., Hair, J. W., Woods, R. K., Jonsson, H. H., Flagan, R. C., Seinfeld, J. H., and
978 Sorooshian, A.: Biomass Burning Plumes in the Vicinity of the California Coast: Airborne Characterization of
979 Physicochemical Properties, Heating Rates, and Spatiotemporal Features, *Journal of Geophysical Research:*
980 *Atmospheres*, 123, 10.1029/2018jd029134, 2018.
- 981 Mass, C. F. and Albright, M. D.: Coastal Southerlies and Alongshore Surges of the West Coast of North America:
982 Evidence of Mesoscale Topographically Trapped Response to Synoptic Forcing, *Monthly Weather Review*, 115,
983 1707-1738, [https://doi.org/10.1175/1520-0493\(1987\)115<1707:CSAASO>2.0.CO;2](https://doi.org/10.1175/1520-0493(1987)115<1707:CSAASO>2.0.CO;2), 1987.
- 984 Mass, C. F. and Steenburgh, W. J.: An Observational and Numerical Study of an Orographically Trapped Wind
985 Reversal along the West Coast of the United States, *Monthly Weather Review*, 128, 2363-2397,
986 [https://doi.org/10.1175/1520-0493\(2000\)128<2363:AOANSO>2.0.CO;2](https://doi.org/10.1175/1520-0493(2000)128<2363:AOANSO>2.0.CO;2), 2000.
- 987 Maudlin, L. C., Wang, Z., Jonsson, H. H., and Sorooshian, A.: Impact of wildfires on size-resolved aerosol
988 composition at a coastal California site, *Atmospheric Environment*, 119, 59-68, 10.1016/j.atmosenv.2015.08.039,
989 2015.
- 990 McNeill, V. F.: Aqueous Organic Chemistry in the Atmosphere: Sources and Chemical Processing of Organic
991 Aerosols, *Environmental Science & Technology*, 49, 1237-1244, 10.1021/es5043707, 2015.
- 992 Melton, C., Washburn, L., and Gotschalk, C.: Wind relaxations and poleward flow events in a coastal upwelling
993 system on the central California coast, *Journal of Geophysical Research: Oceans*, 114, 10.1029/2009jc005397, 2009.
- 994 Monahan, E. C., Spiel, D. E., and Davidson, K. L.: A Model of Marine Aerosol Generation Via Whitecaps and
995 Wave Disruption, in: *Oceanic Whitecaps: And Their Role in Air-Sea Exchange Processes*, edited by: Monahan, E.
996 C., and Niocaill, G. M., Springer Netherlands, Dordrecht, 167-174, 10.1007/978-94-009-4668-2_16, 1986.
- 997 Moorthy, K. K. and Satheesh, S. K.: Characteristics of aerosols over a remote island, Minicoy in the Arabian Sea:
998 Optical properties and retrieved size characteristics, *Quarterly Journal of the Royal Meteorological Society*, 126, 81-
999 109, <https://doi.org/10.1002/qj.49712656205>, 2000.
- 1000 Nuss, W. A.: Synoptic-Scale Structure and the Character of Coastally Trapped Wind Reversals, *Monthly Weather*
1001 *Review*, 135, 60-81, <https://doi.org/10.1175/MWR3267.1>, 2007.
- 1002 Nuss, W. A., Bane, J. M., Thompson, W. T., Holt, T., Dorman, C. E., Ralph, F. M., Rotunno, R., Klemp, J. B.,
1003 Skamarock, W. C., Samelson, R. M., Rogerson, A. M., Reason, C., and Jackson, P.: Coastally Trapped Wind
1004 Reversals: Progress toward Understanding, *Bulletin of the American Meteorological Society*, 81, 719-744,
1005 [https://doi.org/10.1175/1520-0477\(2000\)081<0719:CTWRPT>2.3.CO;2](https://doi.org/10.1175/1520-0477(2000)081<0719:CTWRPT>2.3.CO;2), 2000.



- 1006 Painemal, D. and Zuidema, P.: Assessment of MODIS cloud effective radius and optical thickness retrievals over
1007 the Southeast Pacific with VOCALS-REX in situ measurements, *Journal of Geophysical Research: Atmospheres*,
1008 116, n/a-n/a, 10.1029/2011jd016155, 2011.
- 1009 Parish, T. R.: Forcing of the Summertime Low-Level Jet along the California Coast, *Journal of Applied*
1010 *Meteorology*, 39, 2421-2433, [https://doi.org/10.1175/1520-0450\(2000\)039<2421:FOTSLL>2.0.CO;2](https://doi.org/10.1175/1520-0450(2000)039<2421:FOTSLL>2.0.CO;2), 2000.
- 1011 Pitchford, M., Flocchini, R. G., Draftz, R. G., Cahill, T. A., Ashbaugh, L. L., and Eldred, R. A.: Silicon in
1012 submicron particles in the southwest, *Atmospheric Environment* (1967), 15, 321-333, [https://doi.org/10.1016/0004-6981\(81\)90035-4](https://doi.org/10.1016/0004-6981(81)90035-4), 1981.
- 1014 Prabhakar, G., Ervens, B., Wang, Z., Maudlin, L. C., Coggon, M. M., Jonsson, H. H., Seinfeld, J. H., and
1015 Sorooshian, A.: Sources of nitrate in stratocumulus cloud water: Airborne measurements during the 2011 E-PEACE
1016 and 2013 NiCE studies, *Atmospheric Environment*, 97, 166-173, <https://doi.org/10.1016/j.atmosenv.2014.08.019>,
1017 2014.
- 1018 Pye, H. O. T., Nenes, A., Alexander, B., Ault, A. P., Barth, M. C., Clegg, S. L., Collett Jr, J. L., Fahey, K. M.,
1019 Hennigan, C. J., Herrmann, H., Kanakidou, M., Kelly, J. T., Ku, I. T., McNeill, V. F., Riemer, N., Schaefer, T., Shi,
1020 G., Tilgner, A., Walker, J. T., Wang, T., Weber, R., Xing, J., Zaveri, R. A., and Zuend, A.: The acidity of
1021 atmospheric particles and clouds, *Atmos. Chem. Phys.*, 20, 4809-4888, 10.5194/acp-20-4809-2020, 2020.
- 1022 Rahn, D. A. and Parish, T. R.: Diagnosis of the Forcing and Structure of the Coastal Jet near Cape Mendocino Using
1023 In Situ Observations and Numerical Simulations, *Journal of Applied Meteorology and Climatology*, 46, 1455-1468,
1024 <https://doi.org/10.1175/JAM2546.1>, 2007.
- 1025 Rahn, D. A. and Parish, T. R.: Cessation of the 22–25 June 2006 Coastally Trapped Wind Reversal, *Journal of*
1026 *Applied Meteorology and Climatology*, 49, 1412-1428, <https://doi.org/10.1175/2010JAMC2242.1>, 2010.
- 1027 Ralph, F. M., Armi, L., Bane, J. M., Dorman, C., Neff, W. D., Neiman, P. J., Nuss, W., and Persson, P. O. G.:
1028 Observations and Analysis of the 10–11 June 1994 Coastally Trapped Disturbance, *Monthly Weather Review*, 126,
1029 2435-2465, [https://doi.org/10.1175/1520-0493\(1998\)126<2435:OAAOTJ>2.0.CO;2](https://doi.org/10.1175/1520-0493(1998)126<2435:OAAOTJ>2.0.CO;2), 1998.
- 1030 Reason, C. J. C. and Jury, M. R.: On the generation and propagation of the southern African coastal low, *Quarterly*
1031 *Journal of the Royal Meteorological Society*, 116, 1133-1151, <https://doi.org/10.1002/qj.49711649507>, 1990.
- 1032 Reason, C. J. C., Tory, K. J., and Jackson, P. L.: Evolution of a Southeast Australian Coastally Trapped Disturbance,
1033 *Meteorology and Atmospheric Physics*, 70, 141-165, 10.1007/s007030050031, 1999.
- 1034 Reid, H. J. and Leslie, L. M.: Modeling Coastally Trapped Wind Surges over Southeastern Australia. Part I: Timing
1035 and Speed of Propagation, *Weather and Forecasting*, 14, 53-66, [https://doi.org/10.1175/1520-0434\(1999\)014<0053:MCTWSO>2.0.CO;2](https://doi.org/10.1175/1520-0434(1999)014<0053:MCTWSO>2.0.CO;2), 1999.
- 1037 Rogerson, A. M. and Samelson, R. M.: Synoptic Forcing Of Coastal-Trapped Disturbances in the Marine
1038 Atmospheric Boundary Layer, *Journal of Atmospheric Sciences*, 52, 2025-2040, [https://doi.org/10.1175/1520-0469\(1995\)052<2025:SFOCTD>2.0.CO;2](https://doi.org/10.1175/1520-0469(1995)052<2025:SFOCTD>2.0.CO;2), 1995.
- 1040 Rolph, G., Stein, A., and Stunder, B.: Real-time Environmental Applications and Display sYstem: READY,
1041 *Environmental Modelling & Software*, 95, 210-228, <https://doi.org/10.1016/j.envsoft.2017.06.025>, 2017.
- 1042 Russell, L. M., Sorooshian, A., Seinfeld, J. H., Albrecht, B. A., Nenes, A., Ahlm, L., Chen, Y.-C., Coggon, M.,
1043 Craven, J. S., Flagan, R. C., Frossard, A. A., Jonsson, H., Jung, E., Lin, J. J., Metcalf, A. R., Modini, R.,
1044 Mülmenstädt, J., Roberts, G., Shingler, T., Song, S., Wang, Z., and Wonaschütz, A.: Eastern Pacific Emitted
1045 Aerosol Cloud Experiment, *Bulletin of the American Meteorological Society*, 94, 709-729, 10.1175/bams-d-12-00015.1, 2013.
- 1047 Schlosser, J. S., Braun, R. A., Bradley, T., Dadashazar, H., Macdonald, A. B., Aldhaif, A. A., Aghdam, M. A.,
1048 Mardi, A. H., Xian, P., and Sorooshian, A.: Analysis of aerosol composition data for western United States wildfires
1049 between 2005 and 2015: Dust emissions, chloride depletion, and most enhanced aerosol constituents, *Journal of*
1050 *Geophysical Research: Atmospheres*, 122, 8951-8966, 10.1002/2017jd026547, 2017.
- 1051 Skamarock, W. C., Rotunno, R., and Klemp, J. B.: Models of Coastally Trapped Disturbances, *Journal of the*
1052 *Atmospheric Sciences*, 56, 3349-3365, [https://doi.org/10.1175/1520-0469\(1999\)056<3349:MOCTD>2.0.CO;2](https://doi.org/10.1175/1520-0469(1999)056<3349:MOCTD>2.0.CO;2),
1053 1999.
- 1054 Sorooshian, A., Wang, Z., Coggon, M. M., Jonsson, H. H., and Ervens, B.: Observations of Sharp Oxalate
1055 Reductions in Stratocumulus Clouds at Variable Altitudes: Organic Acid and Metal Measurements During the 2011
1056 E-PEACE Campaign, *Environmental Science & Technology*, 47, 7747-7756, 10.1021/es4012383, 2013.
- 1057 Sorooshian, A., Macdonald, A. B., Dadashazar, H., Bates, K. H., Coggon, M. M., Craven, J. S., Crosbie, E., Hersey,
1058 S. P., Hodas, N., Lin, J. J., Negrón Marty, A., Maudlin, L. C., Metcalf, A. R., Murphy, S. M., Padró, L. T.,
1059 Prabhakar, G., Rissman, T. A., Shingler, T., Varutbangkul, V., Wang, Z., Woods, R. K., Chuang, P. Y., Nenes, A.,
1060 Jonsson, H. H., Flagan, R. C., and Seinfeld, J. H.: A multi-year data set on aerosol-cloud-precipitation-meteorology
1061 interactions for marine stratocumulus clouds, *Scientific Data*, 5, 180026, 10.1038/sdata.2018.26, 2018.



1062 Sorooshian, A., Anderson, B., Bauer, S. E., Braun, R. A., Cairns, B., Crosbie, E., Dadashazar, H., Diskin, G.,
1063 Ferrare, R., Flagan, R. C., Hair, J., Hostetler, C., Jonsson, H. H., Kleb, M. M., Liu, H., Macdonald, A. B.,
1064 McComiskey, A., Moore, R., Painemal, D., Russell, L. M., Seinfeld, J. H., Shook, M., Smith, W. L., Thornhill, K.,
1065 Tselioudis, G., Wang, H., Zeng, X., Zhang, B., Ziemba, L., and Zuidema, P.: Aerosol–Cloud–Meteorology
1066 Interaction Airborne Field Investigations: Using Lessons Learned from the U.S. West Coast in the Design of
1067 ACTIVATE off the U.S. East Coast, *Bulletin of the American Meteorological Society*, 100, 1511-1528,
1068 10.1175/bams-d-18-0100.1, 2019.
1069 Sorooshian, A., MacDonald, A. B., Dadashazar, H., Bates, K. H., Coggon, M. M., Craven, J. S., Crosbie, E.,
1070 Edwards, E.-L., Hersey, S. P., Hodas, N., Lin, J. J., Mardi, A. H., Negrón Marty, A., Maudlin, L. C., Metcalf, A. R.,
1071 Murphy, S. M., Padro, L. T., Prabhakar, G., Rissman, T. A., Schlosser, J. S., Shingler, T., Varutbangkul, V., Wang,
1072 Z., Woods, R. K., Chuang, P. Y., Nenes, A., Jonsson, H. H., Flagan, R. C., Seinfeld, J. H., and Stahl, C.: A Multi-
1073 Year Data Set on Aerosol-Cloud-Precipitation-Meteorology Interactions for Marine Stratocumulus Clouds, figshare,
1074 <https://doi.org/10.6084/m9.figshare.5099983.v11>, 2017.
1075 Stahl, C., Cruz, M. T., Bañaga, P. A., Betito, G., Braun, R. A., Aghdam, M. A., Cambaliza, M. O., Lorenzo, G. R.,
1076 MacDonald, A. B., Hilario, M. R. A., Pabroa, P. C., Yee, J. R., Simpas, J. B., and Sorooshian, A.: Sources and
1077 characteristics of size-resolved particulate organic acids and methanesulfonate in a coastal megacity: Manila,
1078 Philippines, *Atmos. Chem. Phys.*, 20, 15907-15935, 10.5194/acp-20-15907-2020, 2020.
1079 Stein, A. F., Draxler, R. R., Rolph, G. D., Stunder, B. J. B., Cohen, M. D., and Ngan, F.: NOAA’s HYSPLIT
1080 Atmospheric Transport and Dispersion Modeling System, *Bulletin of the American Meteorological Society*, 96,
1081 2059-2077, <https://doi.org/10.1175/BAMS-D-14-00110.1>, 2015.
1082 Thompson, W. T., Burk, S. D., and Lewis, J.: Fog and low clouds in a coastally trapped disturbance, *Journal of*
1083 *Geophysical Research: Atmospheres*, 110, 10.1029/2004jd005522, 2005.
1084 Twomey, S.: Pollution and the planetary albedo, *Atmospheric Environment* (1967), 8, 1251-1256,
1085 [https://doi.org/10.1016/0004-6981\(74\)90004-3](https://doi.org/10.1016/0004-6981(74)90004-3), 1974.
1086 Wang, Z., Sorooshian, A., Prabhakar, G., Coggon, M. M., and Jonsson, H. H.: Impact of emissions from shipping,
1087 land, and the ocean on stratocumulus cloud water elemental composition during the 2011 E-PEACE field campaign,
1088 *Atmospheric Environment*, 89, 570-580, <https://doi.org/10.1016/j.atmosenv.2014.01.020>, 2014.
1089 Wang, Z., Mora Ramirez, M., Dadashazar, H., Macdonald, A. B., Crosbie, E., Bates, K. H., Coggon, M. M., Craven,
1090 J. S., Lynch, P., Campbell, J. R., Azadi Aghdam, M., Woods, R. K., Jonsson, H., Flagan, R. C., Seinfeld, J. H., and
1091 Sorooshian, A.: Contrasting cloud composition between coupled and decoupled marine boundary layer clouds,
1092 *Journal of Geophysical Research: Atmospheres*, 121, 11,679-611,691, 10.1002/2016jd025695, 2016.
1093 Watson, J. G., Chow, J. C., Lowenthal, D. H., Pritchett, L. C., Frazier, C. A., Neuroth, G. R., and Robbins, R.:
1094 Differences in the carbon composition of source profiles for diesel- and gasoline-powered vehicles, *Atmospheric*
1095 *Environment*, 28, 2493-2505, [https://doi.org/10.1016/1352-2310\(94\)90400-6](https://doi.org/10.1016/1352-2310(94)90400-6), 1994.
1096 Winant, C. D., Beardsley, R. C., and Davis, R. E.: Moored wind, temperature, and current observations made during
1097 Coastal Ocean Dynamics Experiments 1 and 2 over the Northern California Continental Shelf and upper slope,
1098 *Journal of Geophysical Research: Oceans*, 92, 1569-1604, <https://doi.org/10.1029/JC092iC02p01569>, 1987.
1099 Wood, R.: Stratocumulus Clouds, *Monthly Weather Review*, 140, 2373-2423, 10.1175/mwr-d-11-00121.1, 2012.
1100 Wu, J.: Bubble flux and marine aerosol spectra under various wind velocities, *Journal of Geophysical Research:*
1101 *Oceans*, 97, 2327-2333, <https://doi.org/10.1029/91JC02568>, 1992.

1102